GEOPHYSICS®

Seismic inversion of shale reservoir properties using microseismic-induced guided waves recorded by distributed acoustic sensing (DAS)

Journal:	*Geophysics*
Manuscript ID	GEO-2020-0607.R3
Manuscript Type:	Technical Paper
Keywords:	DAS (distributed acoustic sensors), microseismic, dispersion, inversion, hydraulic fracturing
Manuscript Focus Area:	Seismic Inversion

Seismic inversion of shale reservoir properties using microseismic-induced guided waves recorded by distributed acoustic sensing (DAS)

Bin Luo[1,*], Ariel Lellouch[2], Ge Jin[1], Biondo Biondi[2], and James Simmons[1]

Right Running Head: DAS microseismic guided-wave inversion

[1]Colorado School of Mines, Department of Geophysics, Golden, Colorado.
E-mail: bluo@mines.edu; gjin@mines.edu; jsimmons@mines.edu.
[2]Stanford University, Geophysics Department, Stanford, California.
E-mail: ariellel@stanford.edu; biondo@stanford.edu.
[*]Now at Stanford University, Geophysics Department, Stanford, California.
E-mail: binluo@stanford.edu.

ABSTRACT

Shale formation properties are crucial for the hydrocarbon production performance of unconventional reservoirs. Microseismic-induced guided waves, which propagate within the low-velocity shale formation, are an ideal candidate for accurate estimation of the shale thickness, velocity, and anisotropy. A DAS fiber deployed along the horizontal section of a monitor well can provide a high-resolution recording of guided waves excited by microseismic events during hydraulic fracturing operations. These guided waves manifest a highly dispersive behavior that allows for seismic inversion of the shale formation properties. An adaptation of the propagator matrix method is presented to estimate guided wave dispersion curves and its accuracy is validated by comparison to 3-D elastic wavefield simulations. The propagator matrix formulation holds for cases of vertical transverse isotropy (VTI) as well. A sensitivity analysis of the theoretical dispersion relations of the guided waves shows that they are mostly influenced by the thickness and S-wave velocity of the low-velocity shale reservoir. The VTI parameters of the formation are also shown to have an impact on the dispersion relations. These physical insights provide the foundation for a dispersion-based model inversion for a 1-D depth-dependent structure of the reservoir and its surroundings. The inversion procedure is validated in a synthetic case and applied to the field records collected in an Eagle Ford hydraulic fracturing project. The inverted structure agrees well with a sonic log acquired several hundred meters away from the monitor well. Seismic inversion using guided wave dispersion therefore shows promise to become a novel and cost-effective strategy for in-situ estimation of reservoir structure and properties, which complements microseismic-based interpretation and production-related information.

INTRODUCTION

Following 20 years' development of horizontal drilling and hydraulic fracturing techniques, shale formations have transitioned from their conventional roles as source rocks and reservoir seals into unconventional roles as important self-sourcing hydrocarbon reservoirs for oil and gas production. Describing and measuring shale formation properties has become vital to determine the quality and volume of these unconventional shale reservoirs and to evaluate the development economics of the shale plays. Conventional surface-based reflection seismology, however, despite successful application in the exploration and development of oil and gas fields, has limited vertical seismic resolution to discriminate thin-bedded hydrocarbon reservoirs with a thickness less than 1/4 wavelength (typically a few tens of meters). Below this thickness, reflections from the top and base interfaces of thin beds start to interfere and can no longer be imaged separately. The amplitude tuning method exploiting the linearity between the interfering reflection amplitude and the bed thickness below 1/8 wavelength (*Widess*, 1973) provides an alternative solution for bed thickness measurement but suffers from large uncertainty. The sparsity of well logs also imposes a challenge to map the shale formation thickness with a fine spatial resolution for local production prediction. New geophysical tools are needed in order to provide accurate information for shale reservoir characterization to aid production-related decision making.

A possible approach to shale reservoir characterization uses guided waves propagating within the shale formation. Deep guided waves have been previously investigated in different geophysical scenarios. An early practical application of guided waves was the detection of discontinuities in coal seams (e.g., *Krey*, 1963; *Buchanan*, 1978; *Dobróka*, 1987). These studies focused on the so-called channel waves that propagate in a horizontal low-velocity coal seam

structure between layers of stiffer rocks. Another geophysical application was cross-well continuity mapping (e.g., *Krohn*, 1992; *Chon et al.*, 1996) which exploited guided waves trapped in geologic formations to indicate reservoir continuity/discontinuity between source and receiver wells to optimize reservoir production. Other studies investigated trapped waves in the damaged zone along a large-scale fault interface, such as the vertical strike-slip San Andreas Fault (e.g., *Ben-Zion and Aki*, 1990; *Li and Vidale*, 1996; *Igel et al.*, 1997). The damaged fault zone is usually more compliant than surrounding rocks due to its fractured nature. Guided waves have also been analyzed and modeled in fluid-filled structures, in the form of tube waves in borehole acoustics (e.g., *Paillet and White*, 1982; *Kurkjian et al.*, 1994) and Krauklis waves in fractures filled with fluid (e.g., *Frehner*, 2014; *Liang et al.*, 2017). In these examples, propagation is within a waveguide that is a natural low-velocity layer (LVL) embedded between high-velocity layers. Recent studies (*Lellouch et al.*, 2019; *Lellouch et al.*, 2020) have shown that perforation-induced guided waves can be observed in an unconventional reservoir with very high resolution (up to 700 Hz) using a horizontal fiber-optic cable interrogated with distributed acoustic sensing (DAS) technology.

Seismic acquisition using DAS has been gaining popularity in applied geophysics in recent years. DAS transforms a fiber-optic cable into a dense distributed strain sensor that enables seismic wavefield detection along the entire cable (*Lumens*, 2014). Fiber-optic cables installed behind casing can tolerate the harsh temperature and pressure conditions in a wellbore, and allow for long-term seismic monitoring without limiting production operations. Downhole installation of DAS fiber allows for various seismic applications, such as vertical seismic profiling (*Mateeva et al.*, 2014; *Daley et al.*, 2016), time-lapse active surveys (*Byerley et al.*, 2018; *Binder et al.*, 2020),

direct measurements of low-frequency strain induced by fracture opening (*Jin and Roy*, 2017), and microseismic monitoring (*Karrenbach et al.*, 2019).

Deployment of fiber-optic cables along the horizontal section of monitor wells in unconventional reservoirs provides a unique setup for high-resolution acquisition of guided waves. Guided waves are primarily confined to the reservoir and cannot be observed by surface receivers. While vertical boreholes can sense them, guided waves propagating into the formation would be sampled only at a single horizontal point. As they travel horizontally along the shale formation and decay rapidly outside the structure, downhole fiber-optic cables deployed horizontally inside or close to the formation can coherently follow their propagation and achieve high-resolution acquisition.

Both perforation shots and microseismic events originating in the low-velocity layer associated with fracture opening/slip during hydraulic fracturing operations can excite guided waves. An example of a microseismic DAS record with strong guided-wave energy is shown in Figure 1, together with its corresponding frequency-wavenumber spectrum. The event was located near the toe of the treatment well and observed by the DAS fiber in the monitor well. The monitor well was drilled into the formation above the targeted shale reservoir, therefore, direct body waves mostly propagate in that formation and show corresponding seismic velocities in the DAS record. The event also generated guided waves that are clearly visible in the horizontal section of the DAS record, suggesting their horizontal propagation within the shale formation. At the heel of the monitor well, the DAS fiber gradually changes its axial orientation from horizontal to vertical, picking up some vertical components of shear waves and guided waves that are evidently coherent over the transition. The guided waves propagate with velocities slower than P and S body waves as shown by the two apparent linear branches marked in the frequency-wavenumber domain. Each

frequency-wavenumber point on these branches has a phase velocity of $c_p = \omega/k$ (where ω and k are angular frequency and angular wavenumber, respectively) that is lower than the S-wave velocity and decreases with frequency. This observation represents the dispersive nature of the guided waves. A more detailed description of guided wave properties is provided by *Lellouch et al.* (2020).

The dispersive characteristics of guided wave propagation are controlled by the rock properties of the multilayered structure, which is similar to other types of boundary waves such as surface waves (at boundaries between vacuum and solid), Stoneley waves (at boundaries between contrasting materials), and Scholte waves (at boundaries between fluid and solid) (*Aki and Richards*, 2002). These rock properties include the elastic parameters and the thickness of the various layers. For an unconventional reservoir, the low-velocity layer is usually the shale formation. Shale formations often exhibit strong anisotropy, especially vertical transverse isotropy (VTI) with horizontal planes of symmetry due to the intrinsic lamination (e.g., *Backus*, 1962; *Vahid and Ahmad*, 2011; *Chertov*, 2012; *Sayers*, 2013; *Sone and Zoback*, 2013). The degree of VTI anisotropy, which can be quantified by the Thomsen parameters (*Thomsen*, 1986), can potentially impact guided wave propagation as well.

This paper investigates the physics behind guided wave dispersion and presents a guided-wave-based inversion procedure to obtain structural information of the unconventional reservoir (shale formation thickness, 1-D S-wave velocity profile, and magnitude of VTI anisotropy) from microseismic-induced guided waves in multichannel DAS records. We first present the propagator matrix method to model the guided wave dispersion curves. Then we conduct 3-D elastic wavefield simulations to reproduce the guided waves in both isotropic and VTI LVL generated by a double-couple microseismic source to validate the accuracy of the propagator matrix method in predicting

guided wave dispersion relations. We perform Monte Carlo inversion for 1-D structure retrieval and analyze the dominant model parameters that control guided wave dispersion relations. The guided-wave-based seismic inversion opens a new path for in-situ measurement of the local unconventional reservoir structure and provides co-located records of geologic parameters and well production/completion data at each individual well.

THEORY AND MODELING

Downhole DAS acquisition of microseismic guided waves

A natural framework to represent guided waves emitted from a point source in a vertically stratified structure is the cylindrical coordinate system, defined by radial, transverse, and vertical coordinates (r, ϕ, z) and the corresponding basis vectors $\hat{\mathbf{r}}$, $\hat{\boldsymbol{\phi}}$, and $\hat{\mathbf{z}}$ (*Aki and Richards*, 2002; *Ursin and Stovas*, 2002). Guided waves radiated from the point source propagate horizontally in the radial direction as cylindrical waves with a circularly symmetric wavefront. In isotropic or VTI media, guided waves consist of two categories, the guided P-SV waves and the guided SH waves. The guided P-SV waves polarize in the r-z plane (radial and vertical) while the guided SH waves polarize in the $\hat{\boldsymbol{\phi}}$ direction (transverse), analogous to the Rayleigh and Love waves in the surface wave categories, respectively.

Similar to the observation of mixed Rayleigh and Love waves in a surface DAS array (*Martin and Biondi*, 2017; *Luo et al.*, 2020), a horizontal downhole DAS fiber that is not in the same vertical plane with the source in the shale formation would potentially observe a mix of both types of guided waves. The DAS channels are in essence a single-component sensor optimally sensitive to axial strain along the fiber (*Lumens*, 2014), resulting in the $\cos^2\theta$ angular relation for

longitudinal waves and $\sin 2\theta$ for transverse waves, where θ is the incident angle between propagation direction and the fiber orientation (*Willis et al.*, 2016; *Wu et al.*, 2017; *Binder et al.*, 2020). The recorded signal at a single DAS channel is the average axial strain over a specific distance along the fiber called the gauge length (*Lumens*, 2014). However, a point-sensor approximation applies when the gauge length is a few times shorter than the wavelengths of interest (*Martin*, 2018). We illustrate our analysis of the geometry and the response of a straight DAS fiber to the cylindrical guided waves emitted from a nearby microseismic source in Figure 2. The variable x_{DAS} is the offset from the projection point of the source onto the DAS fiber, and d_H is the horizontal separation between the point source and the fiber. The DAS response with respect to d_H/x_{DAS} (which equals the tangent function of the incident angle θ) indicates a dominant guided SH wave observation near the source and a dominant guided P-SV wave observation for long-offset channels. The analysis indicates the potential mixture of both types of guided waves in the entire DAS records along the fiber. A similar analysis of DAS directional sensitivity to differently polarized body waves was provided by *Baird et al.* (2020) in the context of a homogeneous VTI medium, and one can easily interpret the DAS sensitivity to guided waves by making an analogy between the guided SH waves and the horizontally propagating body SH-waves, an analogy between the radial guided P-SV waves and the horizontally propagating body P-waves, and an analogy between the vertical guided P-SV waves and the horizontally propagating SV-waves, regardless of the relative depth between the source of guided waves and the fiber-optic cable.

Guided waves may be excited by either perforation shots or microseismic events that occur during hydraulic fracturing operations. However, unlike the perforation shots that position directly on the known wellbore position and strike the formation with intense broadband energy (*Lellouch et al.*, 2019), microseismic sources are mostly offset from the wellbore with uncertain distance and

present several challenges for guided wave acquisition. First, guided waves are strong only when the source is located in the LVL. Sources outside the LVL generate weak or no guided wave signals (*Huff et al.*, 2020). Second, guided waves attenuate due to geometrical spreading, absorption, and scattering. Weak and distant microseismic sources may not provide sufficient guided wave energy for detection and analysis, and the frequency band of the observed guided waves is usually below ~100 Hz. Third, the common double-couple mechanism of microseismic events generates more complicated radiation patterns for guided waves than does a simple point force. Certain types of microseismic moment tensors, when combined with the source-receiver configurations and the DAS directional response pattern, can lead to incomplete or even no recording of guided waves. As a consequence, guided waves are not commonly observed in microseismic DAS recordings. In the Eagle Ford project that we present for field study later in this paper, only 20% of microseismic events generate energetic guided wave signals that are available for analysis. Nonetheless, microseismic events are typically numerous and widespread in practice to present sufficient variability in space distribution, and the observed guided waves can provide statistically stable kinematic measurements for further analysis.

Multichannel analysis of guided waves

Numerous surface wave analysis tools have been developed for decades to exploit the dispersive nature of surface waves for multilayered structure inversion. Given the similarity between surface waves and guided waves, these tools can be adapted to guided wave analysis. The most relevant and appropriate surface wave method for unconventional reservoir guided waves observed by DAS with distributed sensors along a downhole fiber-optic cable would be the widely used multichannel analysis of surface waves (MASW) method (*Park et al.*, 1998; *Park et al.*, 1999;

Park et al., 2004). In the spirit of MASW, we propose the multichannel analysis of guided waves (MAGW) procedure, which, analogous to MASW, consists of three main steps: (1) data acquisition, (2) dispersion analysis, and (3) inversion. For data acquisition, the downhole DAS fiber installed along the horizontal wellbore running parallel and located inside or close to the targeted low-velocity shale formation is currently the optimal way to acquire guided wave signals that propagate along the LVL. In fact, DAS acquisition of guided waves may still be effective even in inclined stratified media, as long as the wellbore is drilled parallel to the layers.

MASW was designed to use a 1-D receiver line for an active survey (*Park et al.*, 1999) or a 2-D receiver array for passive surface wave analysis (*Park et al.*, 2004). In both acquisition schemes, surface waves are decomposed into horizontal plane waves of different frequencies. The phase velocity of each frequency is estimated in the time domain by the slope of the matching plane-wave event spanning across multiple channels. Pairs of frequency and phase velocity define the dispersion curves. The same plane-wave decomposition cannot be applied for microseismic-induced guided waves because of their cylindrical radiation from a point source near the monitor well. We devise a modified phase-shift transform following the generalization derived by *Chapman* (1981) for cylindrical wavefields radiated from a point source. In essence, this modified transformation method measures the phase velocity following hyperbolic moveouts in the multichannel records, which can be viewed as the result of a cylindrical wave decomposition of the guided waves. More details are provided in Appendix A.

The inversion step of MAGW searches for the model parameters that generate the theoretical dispersion curves that best fit the measured dispersion curves. A traditional dispersion inversion method involves two steps in the forward calculation: (1) defining the dispersion equation that links the theoretical dispersion curves to any given multilayered model and (2)

solving this equation for dispersion curves (*Ke et al.*, 2011). We implement the first step using the propagator matrix method, which we discuss in the next section. The second step involves numerical root-finding algorithms to solve the non-linear dispersion equation. The inversion algorithm adjusts the model parameters iteratively to minimize the difference between the theoretical dispersion curves and the dispersion measurements from the data. However, in this study, we adopt the multimodal Monte Carlo inversion algorithm (*Maraschini et al.*, 2010; *Maraschini and Foti*, 2010) which defines an objective function directly based on the dispersion equation and avoids root-finding for dispersion curves. The algorithm was devised for surface wave inversion but a similar idea had initially been proposed for long-wavelength shallow guided wave correction in surface records by *Ernst* (2007). In this algorithm, dropping the root-finding step enables both automatic identification of multimodal dispersion curves and fast computation of the objective function of any given model. These advantages allow for global minimization of searching a large number of random models generated by a stochastic process such as the Monte Carlo sampling method, as shown to be effective for 1-D structure estimation in various studies (*Socco and Boiero*, 2008; *Maraschini and Foti*, 2010; *Dou et al.*, 2017; *Ajo-Franklin et al.*, 2019; *Luo et al.*, 2020). Nevertheless, an adaptation of the dispersion equation in the multimodal inversion algorithm is required as the free surface condition does not hold for deep guided waves.

Propagator matrix method

We briefly summarize the well-studied propagator matrix method for boundary wave study. Wave propagation in horizontally homogeneous multilayered media is governed by the equations of motion and Hooke's law. After applying Fourier transform in time domain and appropriate transformation in the radial direction (Fourier transform for plane wave approximation

or Hankel transform for cylindrical wave approximation), the governing equations can be converted to a set of linear differential equations in terms of the displacement-stress vector $\mathbf{f}(z)$ (*Aki and Richards*, 2002; *Ursin and Stovas*, 2002):

$$\frac{d\mathbf{f}}{dz} = \mathbf{A}\mathbf{f}, \tag{1}$$

where $\mathbf{A}$ is a matrix related to angular frequency ω, horizontal angular wavenumber k, and the z-dependent elastic parameters and density.

For the multilayered isotropic media, equation (1) decouples into two sets of equations, the P-SV equations and the SH equations (*Dunkin*, 1965; *Liu et al.*, 2012), predicting the guided P-SV waves and the guided SH waves, respectively. The same decomposition is also true for VTI layers, and we use the same P-SV and SH notations for the qP-qSV and qSH cases for simplicity. An elastic and isotropic solid body is described by two independent parameters, the P- and S-wave speeds V_P and V_S. A VTI body requires five independent parameters, which are the elastic moduli c_{11}, c_{13}, c_{33}, c_{44}, c_{66} (*Mavko et al.*, 2009), or alternatively, the two wave velocities along the axis of symmetry V_{P0} and V_{S0} together with the three Thomsen anisotropy parameters ε, δ, and γ (*Thomsen*, 1986). The Thomsen parameters describe how the seismic velocity varies with the angle between the wave propagation direction and the axis of symmetry. Useful approximations for purely horizontal propagation in a weak VTI body are that the quasi-P velocity is $V_P \approx V_{P0}(1+\varepsilon)$, the quasi-SV velocity is $V_{SV} \approx V_{S0}$, and quasi-SH velocity is $V_{SH} \approx V_{S0}(1+\gamma)$.

For a given ω, nontrivial solutions to equation (1) under the guided wave boundary conditions exist only when k equals to discrete values k_m (subscript m denotes mode number), and the corresponding nontrivial solution $\mathbf{f}_m(z)$ is the depth-dependent displacements and stresses at the guided-wave front. The most frequently used method to find k_m and its corresponding

nontrivial solution $\mathbf{f}_m(z)$ is the propagator matrix method, which has been intensively studied since the initial work of *Thomson* (1950), *Haskell* (1953), and *Gilbert and Backus* (1966). The original propagator matrix approach formulates the dispersion equation as

$$\det\left(\mathbf{U}^{\mathrm{T}}\mathbf{P}\mathbf{V}\right) = 0 \tag{2}$$

where matrix $\mathbf{P}$ is the product of the propagator matrices of all layers in an n-layered model, $\mathbf{U}$ and $\mathbf{V}$ are matrix representations of the boundary conditions at the top and the base of the entire structure, respectively. *Buchen and Ben-Hador* (1996) documented several distinct surface-wave computation methods in stratified isotropic media and showed their implicit connection with the original Thomson-Haskell propagator matrix method.

The main difference between different types of boundary waves stems from the boundary condition matrices $\mathbf{U}$ and $\mathbf{V}$. For example, when $\mathbf{U}$ describes a free surface condition and $\mathbf{V}$ describes a half-space condition, the resulting equation predicts surface wave dispersion. When both $\mathbf{U}$ and $\mathbf{V}$ describes a free surface condition, the equation predicts Lamb wave behavior in a thin plate. For guided waves, both $\mathbf{U}$ and $\mathbf{V}$ describe an infinite half-space boundary condition. Appendix B provides more details on the propagator matrix and the boundary condition matrices. A generalized expression of $\mathbf{U}$ derived for guided waves is included, which allows one to easily transfer existing surface wave propagator matrix methods to guided wave propagator matrix methods under any notation systems.

Previous studies have provided analytical guided wave dispersion equations for specific cases. *Lowe* (1995) provided the basics of the matrix technique for the P-SV mode of guided ultrasonic waves in multilayered isotropic media bounded by either vacuum or solid. *Buchen and Ben-Hador* (1996) provided the explicit expressions for the boundary matrices $\mathbf{U}$ and $\mathbf{V}$ for both

P-SV and SH modes in multilayered isotropic media. In Appendix C, we show that an exact analytical solution can be found for guided SH waves in a single VTI low-velocity layer. For more structurally complex cases, numerical root-finding algorithms (e.g., *Lowe*, 1995) are needed for multimodal dispersion curve computation as they cannot be estimated analytically.

Propagator matrix validation using 3-D elastic wavefield modeling

A direct solution of the elastic wave equation accurately reproduces the phase and amplitude of the seismic wavefield propagating in a given medium. Whereas full wavefield modeling is computationally expensive and thus prohibitive for dispersion-curve inversion, it is an ideal tool to verify the propagator matrix method for dispersion calculation. We conduct 3-D elastic modeling of guided waves in a three-layered model using an elastic finite-difference modeling operator from the Madagascar package (*Fomel et al.*, 2013). The model consists of a single LVL embedded between a top and a bottom half-space (Figure 3a). All layers are elastic and isotropic. The model parameters include P-wave velocity V_P, S-wave velocity V_S, density ρ, and layer thickness h. A spread of three-component velocity receivers is placed along a horizontal line along the x-axis covering a total length of 1200 m. The depth of the receiver line is 10.5 m above the upper interface, mimicking the monitor well in the field example we show later. Receiver spacing is 1.5 m and sampling rate is 2000 Hz. A double-couple point source is located in the LVL, 12 m below the upper interface.

We first study a simple source-receiver layout where the point source is located in the same vertical plane with the receiver line. In order to study the dispersion behavior of guided P-SV waves and guided SH waves individually, we choose two types of moment tensors, one with

excitation in the M_{xz} component (Figure 3b) and the other with excitation in the M_{yz} component (Figure 3c). Our preliminary analysis of guided wave radiation patterns show that the purposely chosen M_{xz} and M_{yz} excitation can generate strong guided P-SV and guided SH waves, respectively, along the 1-D receiver spread. The M_{xz} excitation generates guided waves propagating along the receiver spread with strong vertical and in-line motions, which favors observation of the guided P-SV waves (in the x- z plane). The M_{yz} excitation, on the contrary, favors guided SH wave propagation with strong transverse motion in the y-direction. While the two types of source mechanisms are purposely chosen for our stated convenience, we remark that an in-depth study of the impact of source mechanism on guided wave behaviors, which involves source orientation, source depth, and guided wave eigenfunctions, can provide important guidance for further analysis of guided waves recorded by DAS and lead to potential retrieval of source parameters. In addition to the two cases with a simple source-receiver layout, we also study a more realistic source-receiver layout for cross-well microseismic monitoring, in which a source with an M_{xz} excitation is located at a certain horizontal offset from the monitor well (Figure 3d). In this case, the recording along the receiver line is expected to be a mix of both guided P-SV and guided SH waves as shown by our analysis in Figure 2. In all cases, sources are broadband single impulses with frequency content from 10 to 150 Hz.

The synthetic common shot gathers and the corresponding dispersion images of the two simulations of the isotropic LVL model are shown in Figure 4. In the shot gather with an M_{xz} excitation, we present the x-component records which correspond to the radial component of the guided P-SV waves. The z-component exhibits similar guided wave patterns and the y-component is zero. Since the source and the receiver line are in the same plane, the x-axis aligns with a radial direction of the cylindrical coordinate system centered at the point source. The guided P-SV

records exhibit a set of linear arrivals, each of which is a single frequency component propagating at a certain phase velocity. These individual phase arrivals form a wave packet whose envelope follows a steeper slope than the individual phase arrivals. The information-carrying envelope propagation speed is described by the group velocity c_g, defined as $d\omega/dk$, as opposed to the phase velocity $c_p = \omega/k$. Similar guided wave patterns can be observed in the shot gather with an M_{yz} excitation, in which we present the y-component displacement corresponding to the transverse component of the guided SH waves.

The modified phase shift method extracts the phase velocity of different frequency components from the synthetic gathers. In these cases, since the sources align with the 1-D receiver line horizontally, the modified phase shift transformation is essentially identical to the 1-D phase shift method by *Park et al.* (1999). Multiple branches of energy peaks are observed in the dispersion image computed from the FD synthetic data. These branches follow precisely the theoretical multimodal curves and prove the validity of the propagator matrix method for both P-SV and SH guided waves. Nonetheless, the propagator matrix approach yields all physically possible dispersion modes. It does not predict which ones will be excited, nor the energy partitioning between the modes. These are affected by the source and the receiver configuration, as well as the excitation term.

We repeat the 3-D FD simulation with a VTI model using the same model parameters and source-receiver layouts shown in Figure 3a-c. The isotropic V_P and V_S values are used as the vertical seismic velocities, V_{P0} and V_{S0}, respectively, for the VTI structure. The Thomsen parameters of the LVL are chosen as $\varepsilon = 0.2$, $\delta = 0.1$, and $\gamma = 0.2$. We maintain the top and bottom half-spaces isotropic, as additional tests suggest the VTI properties of these two layers have little impact on guided wave dispersion behaviors. The resulting dispersion images are shown in

Figure 5. The energetic branches follow the theoretical modal curves and confirm the applicability of the propagator matrix method for VTI cases. The comparison between the isotropic and the VTI models shows a substantial effect of VTI on the dispersion curves with the chosen Thomsen parameters. For guided P-SV waves, although the fundamental curve is barely affected, higher modal curves are shifted toward higher phase velocity because the Thomsen parameters ε and δ define a higher SV-wave velocity in the inclined propagation directions than in the vertical direction (*Thomsen*, 1986). The high-frequency asymptote remains V_{SV} in the horizontal direction, which equals approximately to V_{S0}. For guided SH waves, however, all dispersion curves approach a significantly higher asymptote determined by the horizontal S-wave velocity V_{SH}, which can be approximated to $V_{S0}(1+\gamma)$.

We have studied waveguide properties using idealized pointwise particle velocity measurements where sources and receivers are in the same plane. However, recorded signals can originate from out-of-plane microseismic events. Therefore, we conduct a 3-D FD experiment using the out-of-plane point source shown in Figure 3d to study the effect of a realistic source-receiver layout in microseismic DAS recording. The double-couple focal mechanism is representative of hydraulic fractures oriented perpendicular to the treatment well. We convert the synthetic in-line particle velocity to DAS strain rate along the receiver line using a finite-difference operation (*Bakku*, 2015; *Wang et al.*, 2018; *Binder et al.*, 2020) between receiver pairs separated by a gauge length of 15 m. The finite difference operation is performed every 7.5 m, which determines the DAS channel spacing. Note that the finite difference operation that relates particle velocity to axial strain rate is derived for plane acoustic waves propagating in a homogeneous medium (*Bakku*, 2015). This assumption roughly applies for the synthetic guided waves

propagating in a laterally homogeneous medium when the source-receiver distance is much greater than the gauge length and the wavefront curvature between the receiver pair is negligible.

As predicted by the theoretical analysis of DAS directivity, the resulting synthetic DAS strain rate records exhibit a mix of both guided P-SV and SH modes (Figure 6). We present two dispersion images calculated using different portions of the recording array. Figure 6a shows the dispersion image calculated from the entire DAS profile, along with theoretical dispersion curves of both P-SV and SH guided waves for mode identification. Note that this synthetic result has taken into account the gauge length factor in real DAS observation. The agreement between the energy peaks and the theoretical dispersion curves suggest that a high-fidelity dispersion image can still be obtained for dispersion measurement. The challenge is that the dispersion image shows the mixture of both guided modes. The first two branches of low frequencies and phase velocities are the fundamental and first higher modes of guided P-SV waves, while the other higher modes are of guided SH waves. Nonetheless, we can isolate the guided P-SV waves from the entire records by selecting a long-offset section of the fiber. We choose the channels with x_{DAS} greater than 400 m from the apex and thus $x_{DAS}/d_H > 2$ (Figure 2). The criterion $x_{DAS}/d_H = 2$ is a transition point beyond which $\cos^2\theta > \sin 2\theta$. As such, guided P-SV modes are expected to be dominant in terms of array sensitivity. Figure 6b shows the dispersion image calculated from such a section of the DAS array. Most of the guided wave energy lies along the theoretical guided P-SV dispersion curves, except for a small portion near 150 Hz that belongs to the guided SH waves. The result is of practical importance as choosing the long-offset channels limits the interference of guided SH waves and allows for a separate guided P-SV dispersion analysis. In practice, a long-offset criterion more conservative than $x_{DAS}/d_H > 2$ can be chosen, but the trade-off is that a fiber section of shorter length (36% in this case) provides a lower resolution in the dispersion image.

Figure 6 illustrates that the branches in the dispersion image using the long-offset channels only are wider than those in the dispersion image when using the entire DAS array.

Synthetic data inversion

The multimodal Monte Carlo inversion algorithm defines an objective function $S(\mathbf{m})$ as the L1-norm of $D(\omega, c_p, \mathbf{m})$ where D is the matrix determinant $\det(\mathbf{U}^{\mathrm{T}}\mathbf{PV})$ in equation (2) at the dispersion picks (pairs of ω and c_p), and $\mathbf{m}$ is the multivariate vector of model parameters (*Maraschini et al.*, 2010; *Maraschini and Foti*, 2010). Specifically, the model parameters in $\mathbf{m}$ we use for VTI guided P-SV wave dispersion inversion include vertical S-wave velocity V_{S0}, vertical P-wave velocity V_{P0}, Thomsen parameters (ε and δ), and layer thickness h of each homogeneous layer. Density ρ is not inverted for but estimated from V_{P0} through the empirical relation regressed from a compilation of common lithologies (*Brocher*, 2005). The objective function $S(\mathbf{m})$ is based directly on the propagator matrix determinant D and avoids root-finding for dispersion curves. Global minimization of $S(\mathbf{m})$ is achieved by trying a large number of random models generated by a Monte Carlo process as shown in previous studies (*Socco and Boiero*, 2008; *Maraschini and Foti*, 2010; *Dou et al.*, 2017; *Ajo-Franklin et al.*, 2019).

We test the inversion algorithm based on the guided wave propagator matrix determinant using the synthetic strain rate data generated by an out-of-plane double-couple source in a VTI model. Dispersion picks are obtained automatically by picking the energy peaks in the dispersion image from Figure 6b. The long-offset criterion ensures the guided P-SV modes dominate on the dispersion image. We select the first three branches of the dispersion image and use them for inversion. The Monte Carlo method starts with a sampling pool of 10^7 models randomly selected

between given boundaries. The top 10^3 models with the lowest value of $S(\mathbf{m})$ are considered an ensemble of equivalent models that yield the best-fit for the dispersion picks. The median and interquartile range of the ensemble are used to estimate the model parameters and their uncertainties. The overall best-fitting model that has the absolute lowest $S(\mathbf{m})$ is also used as another estimator of the model parameters.

In Figure 7a, we show the inversion results for the synthetic example. The true model, which a single LVL of 45 m thickness and 1650 m/s S-wave velocity, is plotted in comparison with the inversion results. The best-fitting model is close to the true model. The median of the equivalently best-fitting ensemble is also close to the true model in the top half-space and LVL, but it deviates from the true bottom half-space by 130 m/s. The equivalent ensemble provides a small interquartile range for the LVL (11 m/s) but a relatively large interquartile range for the top and bottom layers (268 and 410 m/s). The LVL thickness recovered in both best-fitting and ensemble median models are 42.6 and 43.5 m (interquartile range of 4.3 m), both of which are within ~3 m difference from the true thickness of 45 m. The estimated $(\varepsilon - \delta)$ from the best-fitting model is 0.085 and the median value of $(\varepsilon - \delta)$ among the ensemble is 0.126, both of which are close to 0.1 in the true model. We emphasize that there is no guarantee that the true model will be chosen in the Monte Carlo sampling, and it is thus not surprising the exact solution is not retrieved. The theoretical curves predicted by the inverted models (Figure 7b) show that they accurately fit the dispersion picks used during inversion. However, all picks are below 2400 m/s. They provide an accurate estimate of the S-wave velocity and layer thickness of the LVL, but the lack of high-velocity picks leads to poor resolution on the top and bottom half-spaces.

FIELD DATA RESULTS

Microseismic events in the Eagle Ford project

We use downhole DAS data collected during monitoring of the hydraulic fracturing operations conducted in the Eagle Ford unconventional reservoir play in Lavaca County, Texas in 2015. The low-velocity Eagle Ford Shale is overlain by the Austin Chalk and underlain by the Buda Limestone (*Condon and Dyman*, 2006), both of which have higher velocities than the Eagle Ford. The treatment well targeted the Eagle Ford Shale and the monitor well targeted the lower Austin Chalk. The horizontal sections of the two wells, with a total length of ~1600 m, are parallel to each other, offset by 30 m vertically and 200 m laterally (Figure 8). A downhole DAS fiber was deployed along the monitor well for seismic acquisition, using a channel spacing of 8 m and a sampling rate of 2000 Hz. The gauge length used for DAS acquisition in this study is 14 m. It is a few times shorter than the wavelengths of the majority of the waves and thus allows for a point-sensor approximation of the distributed strain channels (*Martin*, 2018). The DAS fiber continuously recorded the cross-well microseismic activity during the 15 stages of hydraulic fracturing operations in the treatment well. Microseismic events were also captured by a surface geophone array and underwent standard industry processing, yielding a catalog of 959 events with locations and magnitudes. The horizontal locations of the microseismic events are estimated from the surface geophones as shown in Figure 8.

Field data analysis and inversion

An example of the guided wave dispersion map calculated using the modified phase-shift transform is shown in Figure 9a. The horizontal location of the microseismic event used for

modified phase-shift transformation is obtained from the surface catalog. As we use the long-offset criterion, only guided P-SV modes are visible. We observe multiple dispersion modes that can be clearly identified from 20 to 90 Hz with phase velocities that range between 1800 m/s and 2700 m/s.

In order to improve the consistency of the measured dispersion curves, we select 17 microseismic events from stage 2 and 3 located near the toe of the horizontal treatment well that show visible guided wave signals. These guided waves were generated at early operation stages and propagated from the toe toward the heel of the wellbore through the Eagle Ford formation before it was stimulated. Therefore, we reasonably assume that these guided waves propagated through a horizontally homogeneous medium with potential VTI anisotropy. The aggregated dispersion measurements of the 17 events are statistically consistent and collectively show three apparent dispersion modes between 20 and 90 Hz (Figure 9b) with low variance (< 40 m/s) of the phase velocity.

The multimodal dispersion curves measured from the field records are used in a three-layered model inversion. As shown by the comparison of 1-D vertical S-wave velocity profiles in Figure 10a, the best-fitting model and the ensemble median model show good agreement with a sonic log profile obtained in a vertical well located 500 m from the monitor well (Figure 8). The inverted three-layered model captures the most prominent structure of the Eagle Ford shale formation, with a shale formation thickness of 50.1 m (interquartile range of 4.2 m) and a vertical S-wave velocity of 1639 m/s (interquartile range of 24 m/s). The median value of $(\varepsilon - \delta)$ is 0.46 with a large uncertainty (interquartile range of 0.21). The inverted vertical P-wave profiles are compared with the V_P sonic log in Figure 10b. The results are visually comparable to the log data, but discrepancy exists between the best-fitting and ensemble median results, with a larger

interquartile range of ~300 m/s. The VTI parameters are not precisely determined but the inverted values of $(\varepsilon - \delta)$ in the equivalent ensemble are all greater than 0.2, which necessitates the consideration of strong VTI anisotropy in the Eagle Ford shale formation as shown by previous observations (*White and Sengbush*, 1953; *Miller and Chapman*, 1991; *Chapman and Miller*, 1996; *Sone and Zoback*, 2013; *Mokhtari et al.*, 2016). The theoretical curves of the inverted models are plotted with the dispersion measurements in Figure 10c. The dispersion picks precisely constrain the thickness and S-wave velocity of the Eagle Ford formation. The picks extend up to 2700 m/s, which provides a good constraint on the top layer of Austin Chalk (logged at 2700 m/s). However, the faster bottom layer of the Buda Limestone (logged at 3000 m/s) is poorly constrained.

DISCUSSION

Parameter study of guided wave dispersion curves

The sensitivity of the dispersion curves to the subsurface structure is a crucial element of any dispersion-based inversion procedure. Sensitivity can be evaluated numerically by applying a small perturbation to each model parameter in a given structure and measuring the associated change in the predicted dispersion curves. We first consider the three-layered isotropic model presented in Figure 3a as a reference and study the response of the guided wave dispersion curves to perturbations in the LVL parameters: S-wave velocity V_S, thickness h, P-wave velocity V_P, and density ρ. We apply the small perturbation to one parameter at a time while the other parameters remain unchanged.

Figure 11 shows the sensitivity of the phase velocity of the fundamental, first higher, and second higher modes of the guided P-SV waves with respect to the four isotropic LVL parameters,

calculated as the corresponding partial derivatives multiplied by 1% variation of each parameter from the reference model. In general, sensitivity is not uniform, and large derivatives are localized in a certain frequency band. For higher modes, this band is shifted towards higher frequencies. The derivatives approach zero at high frequencies, except for the ones to V_S which approach 16.5. This value represents exactly 1% of 1650 m/s, which corresponds to the fact that for the high-frequency asymptote, c_p approaches V_S. By comparing the peak values of the phase velocity change, we find that h and V_S are the two key parameters that control the modal curves. In contrast, modal curves are barely sensitive to V_P and ρ. For a 1% increment in the LVL thickness, the phase velocity decreases by 10-15 m/s. For 1% increment in the LVL S-wave velocity, the phase velocity increases by 25-30 m/s. Such a high sensitivity is crucial for the precise inversion of the LVL parameter in guided wave dispersion inversion. The guided SH waves, not shown here, have similar sensitivity patterns to the LVL parameters as the guided P-SV waves, except for the P-wave velocity which has no influence on guided SH dispersion property.

We also evaluate the sensitivity of dispersion curves to the VTI parameters, given $\varepsilon = 0.2$, $\delta = 0.1$, and $\gamma = 0.2$ in the reference LVL. The guided P-SV waves are insensitive to γ and the guided SH waves are insensitive to V_{P0}, ε, and δ. Figure 12 presents the sensitivity of the guided P-SV waves to V_{S0}, V_{P0}, ε, and δ and the sensitivity of guided SH waves to V_{S0} and γ. Both P-SV and SH guided waves are sensitive to changes of V_{S0} but much less so for changes of V_{P0}. Regarding the Thomsen parameters, we notice that they are fractional parameters describing the percentage difference between velocities in different directions, so we evaluate the sensitivity by the partial derivatives multiplied by 1%. The sensitivity of guided P-SV modes to ε and δ are similar but in opposite signs. This can partly be explained by the weak VTI approximation for SV-wave velocity at an inclined angle α from the vertical axis of symmetry: $V_{SV}(\alpha) = V_{S0}$

$\left[1 + V_{P0}^2/V_{S0}^2 \cdot (\varepsilon - \delta) \cdot \sin^2\alpha\cos^2\alpha\right]$ (*Thomsen*, 1986). This relation implies that the two parameters ε and δ cannot be determined independently from the guided P-SV dispersion curves and only $(\varepsilon - \delta)$ can be recovered. This was also shown in previous studies on PP and PS reflection analysis (e.g., *Tsvankin and Grechka*, 2001) where the controlling VTI coefficients $\sigma = V_{P0}^2/V_{S0}^2 \cdot (\varepsilon - \delta)$ and $\eta = (\varepsilon - \delta)/(1 + 2\delta)$ are both linearly related to $(\varepsilon - \delta)$. The sensitivity of guided SH modes to $\Delta\gamma = 1\%$ is nearly flat around 16 m/s, which is ~1% of V_{S0} according to the horizontal propagation approximation of $\partial V_{SH}/\partial\gamma \approx V_{S0}$.

We also examine in detail the response of dispersion curves to the LVL thickness, which is the only geometrical parameter in a single LVL model. In light of the guided SH wave analytical solution (C-4) in Appendix C and the discussion in *Krey* (1963), one can isolate the thickness parameter by defining a dimensionless frequency $\omega h/V_{S0}$. It is also convenient to normalize the phase velocity as c_p/V_{S0}. We compute the theoretical dispersion curves of a set of models with a range of LVL thickness varying from 33 m to 57 m with 4 m increments. Both isotropic and VTI models are considered. The thickness-varying multimodal dispersion curves scaled in terms of the dimensionless frequency and phase velocity are presented in Figure 13. These dispersion curves are identical, suggesting their independence of the LVL thickness, for both guided P-SV modes and SH modes in isotropic and VTI models. The practical implication is that varying the thickness in a single LVL model is equivalent to stretching the modal dispersion curves along the frequency axis. Thus, it does not require any new computation, which is convenient for inversion procedures. The scaling relations together with the steeply descending shape of the curves explain the high sensitivity of the dispersion curves to the layer thickness and S-wave velocity in a single LVL model. A slight change in h^{LVL} perturbs the dispersion curve along the frequency axis, and at the steeply descending part of the curve, such a small stretch along the frequency axis converts to a

relatively large change in the phase velocity axis. Therefore, the steeply descending part of the curve yields high sensitivity to the layer thickness. For more complicated models with multiple layers between the top and bottom half-spaces, such a simple analysis would not apply, and numerical computation of the dispersion curves is necessary.

Guided-wave-based seismic inversion

We use guided waves in downhole DAS records for seismic inversion of shale reservoir properties. The core of the inversion is the physical relation between the multilayered structure and the guided wave dispersion characteristics. We apply this inversion to Eagle Ford microseismic field data, in which the recording well is located outside the low-velocity reservoir. The inverted 1-D model matches reasonably well with sonic log data acquired 500 m away from the production well. Sensitivity analysis of the guided wave dispersion properties shows that given a 10 m/s scale variation in the phase velocity measurements, the inversion yields a meter-scale resolution for layer thickness and 10 m/s scale resolution for S-wave velocity measurements, which can be useful in downhole seismic surveys. The dispersion curves also depend on the VTI parameters. However, detailed analysis not included here suggests that the sensitivity of guided P-SV waves to $(\varepsilon - \delta)$ variation decreases rapidly as the absolute value of $(\varepsilon - \delta)$ increases, which leads to a progressive loss of sensitivity particularly beyond $(\varepsilon - \delta) = 0.2$. This property can partially explain the successful recovery of $(\varepsilon - \delta)$ in the synthetic example, which has weak anisotropy, as well as the large uncertainty of $(\varepsilon - \delta)$ in the field data inversion, as the Eagle Ford Shale probably has much stronger anisotropy.

The guided-wave-based inversion yields average layer properties, estimated along large horizontal propagation distances. While we demonstrate the application of the method on two

consecutive stages, it is possible to apply it in a roll-along fashion to obtain a series of 1-D velocity profiles along the fiber. These profiles can provide reliable information about potential lateral variations of the reservoir thickness and seismic velocity. Time-lapse variation of propagation velocities before and after stimulation may possibly be determined by selecting microseismic events originating at preceding and following hydraulic fracture stages. Also, our research focus is currently limited to the kinematic properties of the guided waves in the phase component and their relation to the velocity structure, rather than studying the whole seismograms. Reproducing realistic amplitude of the guided waves requires accurate knowledge of the source mechanism, attenuation, coupling effects, and exact DAS sensitivity. While these aspects are currently out of the scope of this work, we envision that a full waveform inversion approach in which these aspects are properly addressed to generate reliable synthetic guided wave waveforms can become a promising direction to support guided wave interpretation and yield high-resolution inversion of the velocity structure to benefit hydraulic fracturing operations.

Both synthetic and field data inversion suggests that the anisotropy of the shale formation is a critical elastic property to consider in order to accurately predict guided wave dispersion. The knowledge of VTI anisotropy in the unconventional reservoir has a crucial impact on drilling, completion, and reservoir simulation. For example, *Vahid and Ahmad* (2011) investigated stress distributions around horizontal wells drilled in shales and determined the effect of VTI on fracture initiation pressure and angle. *Chertov* (2012) derived an analytic formula to calculate fracture width in VTI shales and concluded that a complete measurement of anisotropic rock properties is crucial for an accurate estimation of the fracture width. The degree of elastic anisotropy of organic-rich shale is also known to be indicative of the kerogen content in the shale formation (*Sayers*,

2013). The VTI information encoded in guided wave kinematics encourages downhole observations of the seismic wavefield using DAS for well production/completion improvement.

A path to co-located measurement of shale layer properties and well productivity

The relationship between geological information and unconventional reservoir productivity can assist operators in making critical decisions for hydrocarbon production. However, *Tian et al.* (2018) point out that directly linking geological parameters to productivity is challenging since very few wells have both geological and production data. The misalignment of the two types of data arise from the fact that logging wells are vertical wells that usually penetrate through the shale formation whereas the production wells are horizontal wells and turn within the formation. *Tian et al.* (2018) adopt geostatistical methods for geospatial correlation between well measurements to circumvent the difficulty and identify that the depth, thickness, and total organic carbon (TOC) are dominant geological controls of the 6-month cumulative production in the Eagle Ford shale. However, due to the sparsity of the logging wells, the inferred geospatial distribution of shale properties may be far from reality. We argue that the application of guided wave analysis as a downhole seismic tool can directly provide seismic velocity measurements in the vicinity of the production well. Both reservoir thickness and a qualitative magnitude of VTI anisotropy (which can be linked to TOC) can be recovered from the analysis of guided waves excited by either perforation shots or microseismic events. They can be observed by either in-well or cross-well DAS fiber. As downhole DAS deployment has been recently found useful for hydraulic fracture monitoring (*Karrenbach et al.*, 2019), guided wave dispersion analysis can become a useful geophysical tool to provide an in-situ estimation of the elastic properties of the reservoir when guided wave observations are available. Structures obtained from such analysis can potentially

populate co-located records of geological parameters and productivity, augment the database for geostatistical model construction, and guide more accurate predictions in unconventional reservoir productivity.

CONCLUSION

The extensiveness of hydraulic fracturing projects targeting unconventional shale reservoirs requires an accurate description of the shale formation properties. The advent of DAS provides new opportunities for seismic acquisition in the restrictive downhole environment in unconventional reservoirs. A downhole fiber-optic cable installed along a horizontal monitor well can record the dispersive guided waves propagating within the low-velocity shale formation of the unconventional reservoir. We propose a guided-wave-based inversion procedure for reservoir structure estimation. We apply this inversion on the multimodal dispersion curves measured from the guided waves generated by stimulation-induced microseismic events in 3-D synthetic and Eagle Ford field data. This inversion is able to accurately recover reservoir thickness at a single meter scale and seismic velocity at a 10 m/s scale, and can qualitatively point to the magnitude of VTI anisotropy of the shale formation. As the deployment of DAS fibers is becoming more common in unconventional reservoirs, guided wave analysis can become a useful geophysical tool for cost-effective downhole surveys. Potentially, it can allow for the sought-after co-located reservoir properties and production data.

ACKNOWLEDGMENTS

This work was conducted with the support of the Reservoir Characterization Project at Colorado School of Mines. Ariel Lellouch and Biondo Biondi were partially supported through the SEP affiliate program. Ariel Lellouch was partially supported by the Israeli Ministry of Energy under the program for postdoctoral studies in leading universities and by the CoRE (Center of Research Excellence) supported by Chevron. The authors thank Devon Energy and Penn Virginia for providing the microseismic DAS data referenced in this work. Constructive comments from editors and three anonymous reviewers are appreciated.

APPENDIX A

CYLINDRICAL-WAVE PHASE-SHIFT TRANSFROM

Consider a seismic wavefield radiated from a point source at the origin $(0,0)$ of a horizontal 2-D plane, the Fourier transform in two horizontal Cartesian coordinates (x,y) and time t can be expressed in terms of horizontal slowness (p_x,p_y) and angular frequency ω (*Chapman*, 1981) as

$$U(\omega,p_x,p_y) = \int_{-\infty}^{\infty}\int_{-\infty}^{\infty}\int_{-\infty}^{\infty} \exp\left[-i\omega(t-p_x x-p_y y)\right]u(t,x,y)\,dx\,dy\,dt. \qquad \text{(A-1)}$$

Since the wavefield propagates along the radial direction ($\mathbf{p} \parallel \mathbf{x}$), the term $p_x x + p_y y$ can be rewritten as $p\sqrt{x^2+y^2}$, where $p = \sqrt{p_x^2+p_y^2}$ is the total horizontal slowness. Consider N channels on a line along the x-axis with a horizontal distance d_H from the source, then their horizontal

coordinates are (x_j,d_H), $j = 1,2,...,N$. Using the Dirac delta function $\delta(x - x_j, y - d_H)$ for each channel, the integral (A-1) becomes the summation

$$U(\omega,p) = \sum_{j=1}^{N} \exp\left(i\omega p\sqrt{x_j^2 + d_H^2}\right)U(\omega,x_i, d_H), \tag{A-2}$$

where $U(\omega,x_j, d_H)$ is a temporal Fourier transform of the record $u(t,x_j, d_H)$ at channel j. Note that replacing p by the phase velocity $c_p = 1/p$ yields the dispersion image $U(\omega,c_p)$. Comparing (A-2) to the plane-wave phase-shift transformation (*Park et al.*, 1998), we define a hyperbolic phase shift $\exp\left(i\frac{\omega}{c_p}\sqrt{x_j^2 + d_H^2}\right)$ based on the known horizontal source-receiver distance. Grid search of c_p is performed for each ω to find the optimal c_p that aligns the coherent energy of cylindrical waves in the multichannel records.

APPENDIX B

BASICS OF GUIDED WAVE PROPAGATOR MATRIX METHOD

The displacement-stress vector **f** in equation (1) has different forms for different types of guided waves. For guided P-SV waves, $\mathbf{f} = (r_1, r_2, r_3, r_4)^{\mathrm{T}}$ where r_1, r_2 are the radial and vertical displacements, respectively, and r_3, r_4 are the radial and vertical tractions, respectively. For guided SH waves, $\mathbf{f} = (l_1, l_2)^{\mathrm{T}}$ where l_1, l_2 are the transverse displacement and traction, respectively. The propagator matrix $\mathbf{P}_j$ of layer j, deduced from equation (1), is an operator that propagates **f** from depth z_p to z_q within layer j, i.e.,

$$\mathbf{f}(z_p) = \mathbf{P}_j(z_p, z_q)\mathbf{f}(z_q). \tag{B-1}$$

Note that $\mathbf{P}_j$ is a function of ω, k, and a set of model parameters in layer j, including elasticity, density, and depth difference $(z_p - z_q)$. Assuming a welded interface between any two adjacent layers (continuous stresses and displacements), equation (B-1) can be applied recursively from the lower interface of the bottom layer to the upper interface of the top layer, leading to

$$\mathbf{f}(z_0) = \mathbf{P}_1(z_0, z_1)\mathbf{P}_2(z_1, z_2)...\mathbf{P}_n(z_{n-1}, z_n)\mathbf{f}(z_n) = \mathbf{P}(z_0, z_n)\mathbf{f}(z_n), \tag{B-2}$$

where $z_0, z_1, \ldots, z_n$ are the depths of the n+1 layer interfaces of the n layers. At interface z_n, $\mathbf{f}(z_n)$ is converted to a vector $\mathbf{w}_{n+1}$ of upgoing and downgoing wave amplitudes in the bottom half-space by $\mathbf{f}(z_n) = \mathbf{F}_{n+1}\mathbf{w}_{n+1}$, where $\mathbf{w}_{n+1}$ is $(\grave{P}, \grave{S}, \acute{P}, \acute{S})^{\mathrm{T}}$ for P-SV modes and $(\grave{S}, \acute{S})^{\mathrm{T}}$ for SH modes, and $\mathbf{F}_{n+1}$ is a square matrix related to the elasticity and density of the bottom half-space. Since there is no motion at bottom infinity, upgoing waves vanish. The vector $\mathbf{w}_{n+1}$ can be expressed as the product of $\mathbf{B}$ and $\grave{\mathbf{x}}_{n+1}$, where $\mathbf{B} = \begin{bmatrix}1, 0, 0, 0\\ 0, 1, 0, 0\end{bmatrix}^{\mathrm{T}}$ and $\grave{\mathbf{x}}_{n+1} = (\grave{P}, \grave{S})^{\mathrm{T}}$ for P-SV modes, and $\mathbf{B} = (1, 0)^{\mathrm{T}}$ and $\grave{\mathbf{x}}_{n+1} = (\grave{S})$ for SH modes.

For surface waves, the traction-free condition at z_0 requires the zeros stresses in $\mathbf{f}(z_0)$. These terms can be selected by matrix $\mathbf{U}$, which is $\begin{bmatrix}0, 0, 1, 0\\ 0, 0, 0, 1\end{bmatrix}^{\mathrm{T}}$ for Rayleigh waves and $(0, 1)^{\mathrm{T}}$ for Love waves. Using matrix $\mathbf{U}$ and matrix $\mathbf{V} = \mathbf{F}_{n+1}\mathbf{B}$, the traction-free condition can be expressed as

$$\mathbf{U}^{\mathrm{T}}\mathbf{P}(z_0, z_n)\mathbf{V}\grave{\mathbf{x}}_{n+1} = 0. \tag{B-3}$$

The existence of nontrivial solution for $\grave{\mathbf{x}}_{n+1}$ in equation (B-3) requires the determinant of $\mathbf{U}^{\mathrm{T}}\mathbf{PV}$ to be zero, which leads to the dispersion equation (2) for surface waves. Solving equation (2) associated with a given layered model provides the corresponding dispersion relation $k_m(\omega)$.

The same physics for theoretical dispersion computation applies to the buried multilayered structure at depth. In general, the matrix $\mathbf{V}$ is retained for the bottom half-space, and the free-surface condition is replaced by a buried boundary condition underlain by a top half-space, which is no energy entering the LVL. In other words, the downgoing waves in the top half-space must be zero. One can rewrite $\mathbf{f}(z_0)$ in equation (B-2) as $\mathbf{F}_0\mathbf{B}\grave{\mathbf{x}}_0$ in a manner similar to $\mathbf{f}(z_n)$. Then the vanishing downgoing wave boundary condition can be expressed as

$$\grave{\mathbf{x}}_0 = (\mathbf{B})^{-1}(\mathbf{F}_0)^{-1}\mathbf{P}(z_0, z_n)\mathbf{F}_{n+1}\mathbf{B}\grave{\mathbf{x}}_{n+1} = 0 \tag{B-4}$$

Note that $\mathbf{B}$ is a non-square matrix and one should define its left inverse for $(\mathbf{B})^{-1}$, which equals to $\frac{1}{2}\mathbf{B}^{\mathrm{T}}$ for guided P-SV waves and $\mathbf{B}^{\mathrm{T}}$ for guided SH waves. By defining

$$\mathbf{U} = \left[(\mathbf{B})^{-1}(\mathbf{F}_0)^{-1}\right]^{\mathrm{T}}, \tag{B-5}$$

we obtain the dispersion equation for guided waves in the exact same form of equation (2).

For guided P-SV waves, we adopt the derivation of Rayleigh wave propagator matrix representation in VTI media by *Ikeda and Matsuoka* (2013) and modify the boundary condition of the top half-space. Following their notation and our previous discussion, the top boundary matrix for guided P-SV waves in VTI media is

$$\mathbf{U}^{\mathrm{T}} = \frac{1}{2}\begin{bmatrix} -\dfrac{d_4}{d_5} & -\dfrac{\varepsilon_3}{c_{33}d_6} & \dfrac{d_2}{c_{33}d_6} & \dfrac{1}{c_{44}d_5} \\ \dfrac{d_3}{d_5} & \dfrac{\varepsilon_1}{c_{33}d_6} & -\dfrac{d_1}{c_{33}d_6} & -\dfrac{1}{c_{44}d_5} \end{bmatrix}. \tag{B-6}$$

Readers are referred to *Ikeda and Matsuoka* (2013) for notation definition (note that here ε_1 and ε_3 are not the Thomsen parameter ε) and the explicit expressions of matrices $\mathbf{P}$ and $\mathbf{V}$.

APPENDIX C

EXACT DISPERSION SOLUTIONS FOR GUIDED SH MODES IN A THREE-LAYERED VTI MODEL

According to *Ke et al.* (2011), the matrix **A** in equation (1) for SH modes in a VTI body is $\mathbf{A} = \begin{bmatrix} 0 & c_{44}^{-1} \\ -\rho\omega + k^2 c_{66} & 0 \end{bmatrix}$, where ρ is density. Following the derivation in *Aki and Richards* (2002), the propagator matrix **P** for a VTI layer with thickness h is

$$\mathbf{P} = \begin{bmatrix} \cosh \nu h & (c_{44}\nu)^{-1} \sinh \nu h \\ (c_{44}\nu) \sinh \nu h & \cosh \nu h \end{bmatrix}, \tag{C-1}$$

where $\nu = \frac{\omega}{V_{s0}} \sqrt{\frac{V_{SH}^2}{c_p^2} - 1}$ with vertical and horizontal S-wave velocities $V_{S0} = \sqrt{c_{44}/\rho}$ and $V_{SH} = \sqrt{c_{66}/\rho}$, respectively. The boundary condition matrices are

$$\mathbf{U}^{\mathrm{T}} = \frac{1}{2}\begin{bmatrix} 1 & (c_{44}\nu)^{-1} \end{bmatrix}, \tag{C-2}$$

and

$$\mathbf{V}^{\mathrm{T}} = \begin{bmatrix} 1 & c_{44}\nu \end{bmatrix}. \tag{C-3}$$

Consider a three-layered model with one single LVL embedded between a top and a bottom half-space, and without loss of generality, assume $V_{SH,\mathrm{TOP}} < V_{SH,\mathrm{BOT}}$, then the dispersion equation (2) can be solved directly for the phase velocity c_p between $V_{SH,\mathrm{LVL}}$ and $V_{SH,\mathrm{TOP}}$, yielding

$$\omega = \frac{V_{S0,\mathrm{LVL}}}{h}\left(1 - \frac{V_{SH,\mathrm{LVL}}^2}{c_p^2}\right)^{-\frac{1}{2}}\left[\arctan\left(\frac{X_{\mathrm{TOP}}}{X_{\mathrm{LVL}}}\right) + \arctan\left(\frac{X_{\mathrm{BOT}}}{X_{\mathrm{LVL}}}\right) + \pi m\right], \tag{C-4}$$

where $c_p = k/\omega$, $X_{\mathrm{LVL}} = \rho_{\mathrm{LVL}} V_{SV,\mathrm{LVL}} \sqrt{1 - \frac{V_{SH,\mathrm{LVL}}^2}{c_p^2}}$, $X_{\mathrm{TOP}} = \rho_{\mathrm{TOP}} V_{SV,\mathrm{TOP}} \sqrt{\frac{V_{SH,\mathrm{TOP}}^2}{c_p^2} - 1}$, and $X_{\mathrm{BOT}} = \rho_{\mathrm{BOT}} V_{SV,\mathrm{BOT}} \sqrt{\frac{V_{SH,\mathrm{BOT}}^2}{c_p^2} - 1}$. The subscripts LVL, TOP, and BOT denote the layer to which the property belongs (low-velocity layer, top half-space, and bottom half-space, respectively). By setting $V_{SH} = V_{S0}$ for all layers, the general solution (C-4) for a VTI model reduces to the analytical solution for an isotropic three-layered model studied by *Dobróka* (1987) for channel SH waves in a coal seam structure and by *Ben-Zion and Aki* (1990) for trapped SH waves in a low-velocity fault zone. It further reduces to the solution provided by *Krey* (1963) and *Buchanan* (1978) for a symmetric isotropic three-layered model with identical top and bottom half-spaces.

REFERENCES

Ajo-Franklin, J. B., et al. (2019), Distributed Acoustic Sensing Using Dark Fiber for Near-Surface Characterization and Broadband Seismic Event Detection, *Scientific reports*, *9*(1), 1328.

Aki, K., and P. G. Richards (2002), *Quantitative seismology*.

Backus, G. E. (1962), Long‐wave elastic anisotropy produced by horizontal layering, *J. Geophys. Res.*, *67*(11), 4427-4440, doi:10.1029/JZ067i011p04427.

Baird, A., et al. (2020), Characteristics of microseismic data recorded by Distributed Acoustic Sensing (DAS) systems in anisotropic media, *Geophysics*, *85*(4), 1-37, doi:10.1190/geo2019-0776.1.

Bakku, S. K. (2015), Fracture characterization from seismic measurements in a borehole, Massachusetts Institute of Technology.

Ben-Zion, Y., and K. Aki (1990), Seismic radiation from an SH line source in a laterally heterogeneous planar fault zone, *Bull. Seismol. Soc. Am.*, *80*(4), 971-994.

Binder, G., et al. (2020), Modeling the seismic response of individual hydraulic fracturing stages observed in a time-lapse distributed acoustic sensing vertical seismic profiling survey, *Geophysics*, *85*(4), T225-T235.

Brocher, T. M. (2005), Empirical relations between elastic wavespeeds and density in the Earth's crust, *Bull. Seismol. Soc. Am.*, *95*(6), 2081-2092, doi:10.1785/0120050077.

Buchanan, D. (1978), The propagation of attenuated SH channel waves, *Geophysical Prospecting*, *26*(1), 16-28, doi:10.1111/j.1365-2478.1978.tb01575.x.

Buchen, P., and R. Ben-Hador (1996), Free-mode surface-wave computations, *Geophys. J. Int.*, *124*(3), 869-887, doi:10.1111/j.1365-246X.1996.tb05642.x.

Byerley, G., D. Monk, P. Aaron, and M. Yates (2018), Time-lapse seismic monitoring of individual hydraulic frac stages using a downhole DAS array, *The Leading Edge*, *37*(11), 802-810, doi:10.1190/tle37110802.1.

Chapman, C. (1981), Generalized Radon transforms and slant stacks, *Geophys. J. Int.*, *66*(2), 445-453, doi:10.1111/j.1365-246X.1981.tb05966.x.

Chapman, C., and D. Miller (1996), Velocity sensitivity in transversely isotropic media, *Geophysical prospecting*, *44*(3), 525-549, doi:10.1111/j.1365-2478.1996.tb00163.x.

Chertov, M. (2012), Closed-form solution for vertical fracture width in anisotropic elastic formations, *Int J Rock Mech Min*, *53*, 70-75, doi:10.1016/j.ijrmms.2012.04.006.

Chon, Y.-T., W. Turpening, S. Rutherford, and M. Parchman (1996), Reservoir continuity logging using connectivity mapping while drilling, *The Leading Edge*, *15*(3), 203-208, doi:10.1190/1.1437296.

Condon, S., and T. Dyman (2006), 2003 geologic assessment of undiscovered conventional oil and gas resources in the Upper Cretaceous Navarro and Taylor Groups, Western Gulf Province, Texas*Rep. 1411309987*, US Geological Survey.

Daley, T., D. Miller, K. Dodds, P. Cook, and B. Freifeld (2016), Field testing of modular borehole monitoring with simultaneous distributed acoustic sensing and geophone vertical seismic profiles at Citronelle, Alabama, *Geophysical Prospecting*, *64*(5), 1318-1334, doi:10.1111/1365-2478.12324.

Dobróka, M. (1987), Love seam‐waves in a horizontally inhomogeneous three‐layered medium, *Geophysical prospecting*, *35*(5), 502-516, doi:10.1111/j.1365-2478.1987.tb00832.x.

Dou, S., et al. (2017), Distributed acoustic sensing for seismic monitoring of the near surface: A traffic-noise interferometry case study, *Scientific reports*, *7*(1), 11620.

Dunkin, J. W. (1965), Computation of modal solutions in layered, elastic media at high frequencies, *Bull. Seismol. Soc. Am.*, *55*(2), 335-358.

Ernst, F. (2007), Long-wavelength statics estimation from guided waves, paper presented at 69th EAGE Conference and Exhibition incorporating SPE EUROPEC 2007, European Association of Geoscientists & Engineers.

Fomel, S., P. Sava, I. Vlad, Y. Liu, and V. Bashkardin (2013), Madagascar: Open-source software project for multidimensional data analysis and reproducible computational experiments, *Journal of Open Research Software*, *1*(1), doi:10.5334/jors.ag.

Frehner, M. (2014), Krauklis wave initiation in fluid-filled fractures by seismic body waves, *Geophysics*, *79*(1), T27-T35, doi:10.1190/geo2013-0093.1.

Gilbert, F., and G. E. Backus (1966), Propagator matrices in elastic wave and vibration problems, *Geophysics*, *31*(2), 326-332, doi:10.1190/1.1439771.

Haskell, N. A. (1953), The dispersion of surface waves on multilayered media, *Bull. Seismol. Soc. Am.*, *43*(1), 17-34.

Huff, O., A. Lellouch, B. Luo, G. Jin, and B. Biondi (2020), Validating the origin of microseismic events in target reservoir using guided waves recorded by DAS, *The Leading Edge*, *39*(11), 776-784, doi:10.1190/tle39110776.1.

Igel, H., Y. Ben-Zion, and P. C. Leary (1997), Simulation of SH-and P-SV-wave propagation in fault zones, *Geophys. J. Int.*, *128*(3), 533-546.

Ikeda, T., and T. Matsuoka (2013), Computation of Rayleigh Waves on Transversely Isotropic Media by the Reduced Delta Matrix Method, *Bull. Seismol. Soc. Am.*, *103*(3), 2083-2093, doi:10.1785/0120120207.

Jin, G., and B. Roy (2017), Hydraulic-fracture geometry characterization using low-frequency DAS signal, *The Leading Edge*, *36*(12), 975-980.

Karrenbach, M., et al. (2019), Fiber-optic distributed acoustic sensing of microseismicity, strain and temperature during hydraulic fracturing, *Geophysics*, *84*(1), D11-D23, doi:10.1190/geo2017-0396.1.

Ke, G. P., H. F. Dong, A. Kristensen, and M. Thompson (2011), Modified Thomson-Haskell Matrix Methods for Surface-Wave Dispersion-Curve Calculation and Their Accelerated Root-Searching Schemes, *Bull. Seismol. Soc. Am.*, *101*(4), 1692-1703, doi:10.1785/0120100187.

Krey, T. C. (1963), Channel waves as a tool of applied geophysics in coal mining, *Geophysics*, *28*(5), 701-714, doi:10.1190/1.1439258.

Krohn, C. E. (1992), Cross-well continuity logging using guided seismic waves, *The Leading Edge*, *11*(7), 39-45, doi:10.1190/1.1436887.

Kurkjian, A., R. Coates, J. White, and H. Schmidt (1994), Finite-difference and frequency-wavenumber modeling of seismic monopole sources and receivers in fluid-filled boreholes, *Geophysics*, *59*(7), 1053-1064, doi:10.1190/1.1443661.

Lellouch, A., et al. (2019), DAS observations and modeling of perforation-induced guided waves in a shale reservoir, *The Leading Edge*, *38*(11), 858-864, doi:10.1190/tle38110858.1.

Lellouch, A., M. A. Meadows, T. Nemeth, and B. Biondi (2020), Fracture properties estimation using DAS recording of guided waves in unconventional reservoirs, *Geophysics*, *85*(5), 1-59, doi:10.1190/geo2019-0793.1.

Li, Y.-G., and J. E. Vidale (1996), Low-velocity fault-zone guided waves: numerical investigations of trapping efficiency, *Bull. Seismol. Soc. Am.*, *86*(2), 371-378.

Liang, C., O. O'Reilly, E. M. Dunham, and D. Moos (2017), Hydraulic fracture diagnostics from Krauklis-wave resonance and tube-wave reflections, *Geophysics*, *82*(3), D171-D186, doi:10.1190/geo2016-0480.1.

Liu, T., C. Zhao, and Y. Duan (2012), Generalized transfer matrix method for propagation of surface waves in layered azimuthally anisotropic half-space, *Geophys. J. Int.*, *190*(2), 1204-1212, doi:10.1111/j.1365-246X.2012.05547.x.

Lowe, M. J. (1995), Matrix techniques for modeling ultrasonic waves in multilayered media, *IEEE transactions on ultrasonics, ferroelectrics, and frequency control*, *42*(4), 525-542, doi:10.1109/58.393096.

Lumens, P. G. E. (2014), Fibre-optic sensing for application in oil and gas wells, doi:10.6100/IR769555.

Luo, B., et al. (2020), Horizontally orthogonal distributed acoustic sensing array for earthquake- and ambient-noise-based multichannel analysis of surface waves, *Geophys. J. Int.*, *222*(3), 2147-2161, doi:10.1093/gji/ggaa293.

Maraschini, M., F. Ernst, S. Foti, and L. V. Socco (2010), A new misfit function for multimodal inversion of surface waves, *Geophysics*, *75*(4), G31-G43, doi:10.1190/1.3436539.

Maraschini, M., and S. Foti (2010), A Monte Carlo multimodal inversion of surface waves, *Geophys. J. Int.*, *182*(3), 1557-1566, doi:10.1111/j.1365-246X.2010.04703.x.

Martin, E. R. (2018), Passive Imaging and Characterization of the Subsurface with Distributed Acoustic Sensing, Stanford University.

Martin, E. R., and B. L. Biondi (2017), Ambient noise interferometry across two-dimensional DAS arrays, in *SEG Technical Program Expanded Abstracts 2017*, edited, pp. 2642-2646, Society of Exploration Geophysicists.

Mateeva, A., et al. (2014), Distributed acoustic sensing for reservoir monitoring with vertical seismic profiling, *Geophysical Prospecting*, *62*(4), 679-692, doi:10.1111/1365-2478.12116.

Mavko, G., T. Mukerji, and J. Dvorkin (2009), *The Rock Physics Handbook: Tools for Seismic Analysis of Porous Media*, Cambridge University Press.

Miller, D. E., and C. H. Chapman (1991), Incontrovertible evidence of anisotropy in crosswell data, in *SEG Technical Program Expanded Abstracts 1991*, edited, pp. 825-828, Society of Exploration Geophysicists.

Mokhtari, M., M. M. Honarpour, A. N. Tutuncu, and G. N. Boitnott (2016), Characterization of Elastic Anisotropy in Eagle Ford Shale: Impact of Heterogeneity and Measurement Scale, *Spe Reserv Eval Eng*, *19*(3), 429-439, doi:10.2118/170707-Pa.

Paillet, F., and J. White (1982), Acoustic modes of propagation in the borehole and their relationship to rock properties, *Geophysics*, *47*(8), 1215-1228, doi:10.1190/1.1441384.

Park, C., et al. (2004), Imaging dispersion curves of passive surface waves, in *SEG technical program expanded abstracts 2004*, edited, pp. 1357-1360, Society of Exploration Geophysicists, doi:10.1190/1.1851112.

Park, C. B., R. D. Miller, and J. Xia (1998), Imaging dispersion curves of surface waves on multi-channel record, in *SEG Technical Program Expanded Abstracts 1998*, edited, pp. 1377-1380, Society of Exploration Geophysicists, doi:10.1190/1.1820161.

Park, C. B., R. D. Miller, and J. Xia (1999), Multichannel analysis of surface waves, *Geophysics*, *64*(3), 800-808, doi:10.1190/1.1444590.

Sayers, C. M. (2013), The effect of kerogen on the elastic anisotropy of organic-rich shales, *Geophysics*, *78*(2), D65-D74, doi:10.1190/geo2012-0309.1.

Socco, L. V., and D. Boiero (2008), Improved Monte Carlo inversion of surface wave data, *Geophysical Prospecting*, *56*(3), 357-371.

Sone, H., and M. D. Zoback (2013), Mechanical properties of shale-gas reservoir rocks—Part 1: Static and dynamic elastic properties and anisotropy, *Geophysics*, *78*(5), D381-D392, doi:10.1190/geo2013-0050.1.

Thomsen, L. (1986), Weak Elastic-Anisotropy, *Geophysics*, *51*(10), 1954-1966, doi:10.1190/1.1442051.

Thomson, W. T. (1950), Transmission of elastic waves through a stratified solid medium, *Journal of applied Physics*, *21*(2), 89-93, doi:10.1063/1.1699629.

Tian, Y., W. B. Ayers, H. Sang, W. D. McCain Jr, and C. Ehlig-Economides (2018), Quantitative evaluation of key geological controls on regional Eagle Ford shale production using spatial statistics, *Spe Reserv Eval Eng*, *21*(02), 238-256.

Tsvankin, I., and V. Grechka (2001), Parameter estimation for VTI media using PP and PS reflection data, in *SEG Technical Program Expanded Abstracts 2001*, edited, pp. 857-860, Society of Exploration Geophysicists, doi:10.1190/1.1816770.

Ursin, B., and A. Stovas (2002), Reflection and transmission responses of a layered isotropic viscoelastic medium, *Geophysics*, *67*(1), 307-323, doi:10.1190/1.1451803.

Vahid, S., and G. Ahmad (2011), Hydraulic fracture initiation from a wellbore in transversely isotropic rock, paper presented at 45th US Rock Mechanics/Geomechanics Symposium, American Rock Mechanics Association.

Wang, H. F., et al. (2018), Ground motion response to an ML 4.3 earthquake using co-located distributed acoustic sensing and seismometer arrays, *Geophys. J. Int.*, *213*(3), 2020-2036, doi:10.1093/gji/ggy102.

White, J. E., and R. L. Sengbush (1953), Velocity measurements in near-surface formations, *Geophysics*, *18*(1), 54-69, doi:10.1190/1.1437863.

Widess, M. (1973), How thin is a thin bed?, *Geophysics*, *38*(6), 1176-1180, doi:10.1190/1.1440403.

Willis, M. E., et al. (2016), Quantitative quality of distributed acoustic sensing vertical seismic profile data, *The Leading Edge*, *35*(7), 605-609, doi:10.1190/tle35070605.1.

Wu, X., et al. (2017), Compressional-and shear-wave studies of distributed acoustic sensing acquired vertical seismic profile data, *The Leading Edge*, *36*(12), 987-993, doi:10.1190/tle36120987.1.

LIST OF FIGURE CAPTIONS

Figure 1. (a) The DAS seismic profile of an example microseismic event along the fiber in an L-shape monitor well. The black solid vertical line denotes the heel of the well. (b) The frequency-wavenumber spectrum of the horizontal section of the DAS record. Body waves and guided waves are marked. Green line segments in (a) and white dashed lines in (b) mark rough estimates of body P-wave velocity (5100 m/s), body S-wave velocity (2800 m/s), and guided wave group velocity (1500 m/s).

Figure 2. (a) Schematic map view diagram of the propagation geometry of the cylindrical guided waves and (b) the directional response of DAS to different types of guided waves along the DAS fiber.

Figure 3. (a) Cross-section of the three-layered model (not to scale) and parameter summary for 3-D wavefield modeling. (b) Zero-y-offset double-couple point source with an M_{xz} excitation term. (c) Zero-y-offset double-couple point source with an M_{yz} excitation term. (d) Double-couple source with 200 m horizontal y-offset from the receiver line. (b-d) are map views of horizontal source-receiver layouts.

Figure 4. Synthetic seismic profiles of the isotropic model showing (a) x-component particle velocity of the M_{xz} experiment (Figure 3b) and (b) y-component particle velocity of the M_{yz} experiment (Figure 3c). Guided waves are highlighted by the black dashed ellipses. In (a), we observe P-SV modes, whereas in (b) SH modes are present. Reference travel velocities of different seismic modes are provided in (a). The corresponding dispersion images are shown in (c) and (d), respectively. White solid curves denote the theoretical multimodal dispersion curves obtained with the propagator matrix method. Mode numbers from fundamental to fourth are marked.

Figure 5. Dispersion images of the VTI model for synthetic (a) guided P-SV and (b) guided SH waves. White solid curves denote the theoretical multimodal dispersion curves of the VTI model. White dashed curves are the theoretical dispersion curves of the isotropic model for comparison.

Figure 6. Dispersion images calculated from (a) the entire synthetic DAS records and (b) the long-offset synthetic DAS records. The DAS fiber is offset horizontally by 200 m from the source. White solid and black dash-dotted curves are theoretical dispersion curves of guided P-SV and SH waves, respectively, of the VTI LVL model. In (a), the fundamental and first P-SV modes are marked by white arrows, and the guided SH modes are highlighted by a black rectangle.

Figure 7. (a) Comparison of the V_{S0} profiles of the true VTI model (black), the best-fitting model (red dashed) and the median model of the best-fitting ensemble (blue dash-dotted). Light blue area represents the uncertainty range of the best-fitting ensemble. Green dotted lines mark the parameter boundaries for the Monte Carlo inversion. (b) Dispersion picks of the synthetic guided P-SV waves (orange) and the theoretical dispersion curves computed from the three models in (a).

Figure 8. Map view of the microseismic events that occurred during the hydraulic fracturing operations in the Eagle Ford project. Locations were obtained from surface geophone processing. Events are color-coded to indicate whether energetic guided waves are observed (*Huff et al.*, 2020). The horizontal section of the DAS monitor well (red curve), the horizontal section of the treatment well (black curve), and a vertical well (blue square) that was logged are also shown.

Figure 9. (a) Normalized dispersion image of the guided waves of a microseismic event example in the Eagle Ford project. Three trends of energy peaks are marked as fundamental, first higher, and second higher modes. (b) Dispersion picks of 17 microseismic events excited near the toe of the monitor well and displaying clear guided wave signals.

Figure 10. (a) The V_{S0} profile and (b) the V_{P0} profile of the best-fit 1-D model (red dashed) and the median model of the equivalent ensemble (blue dash-dotted). Light blue area shows the uncertainty range. Green dash-dotted curves are parameter boundaries for inversion. The sonic log profile (black solid) is shown for comparison. (c) Theoretical dispersion curves of guided P-SV waves of the best-fit model and the median model of the equivalent ensemble. Dispersion measurements of the Eagle Ford microseismic guided waves (black symbols) are shown for comparison.

Figure 11. Sensitivity of the fundamental, first higher, and second higher modes of the guided P-SV waves with respect to (a) ΔV_S, (b) Δh, (c) ΔV_P, and (d) $\Delta \rho$, each of which is a 1% variation of the corresponding parameter compared to the reference model.

Figure 12. Sensitivity of the fundamental, first, and second guided wave modes to variation of wave velocities (a-c) and Thomsen parameters (d-f) in the LVL. Guided P-SV modal curves are sensitive to (a) vertical S-wave velocity, (b) vertical P-wave velocity, (d) ε, and (e) δ, while guided SH modal curves are sensitive to (c) vertical LVL S-wave velocity and (f) γ.

Figure 13. Dimensionless multimodal dispersion curves of (a) the isotropic models and (b) the VTI models. Each numerically calculated dispersion curve is a stack of overlapping curves calculated from a set of models with various LVL thickness ranging from 33 m to 57 m with 4 m stepping. The analytical solutions for guided SH modes are plotted for comparison.

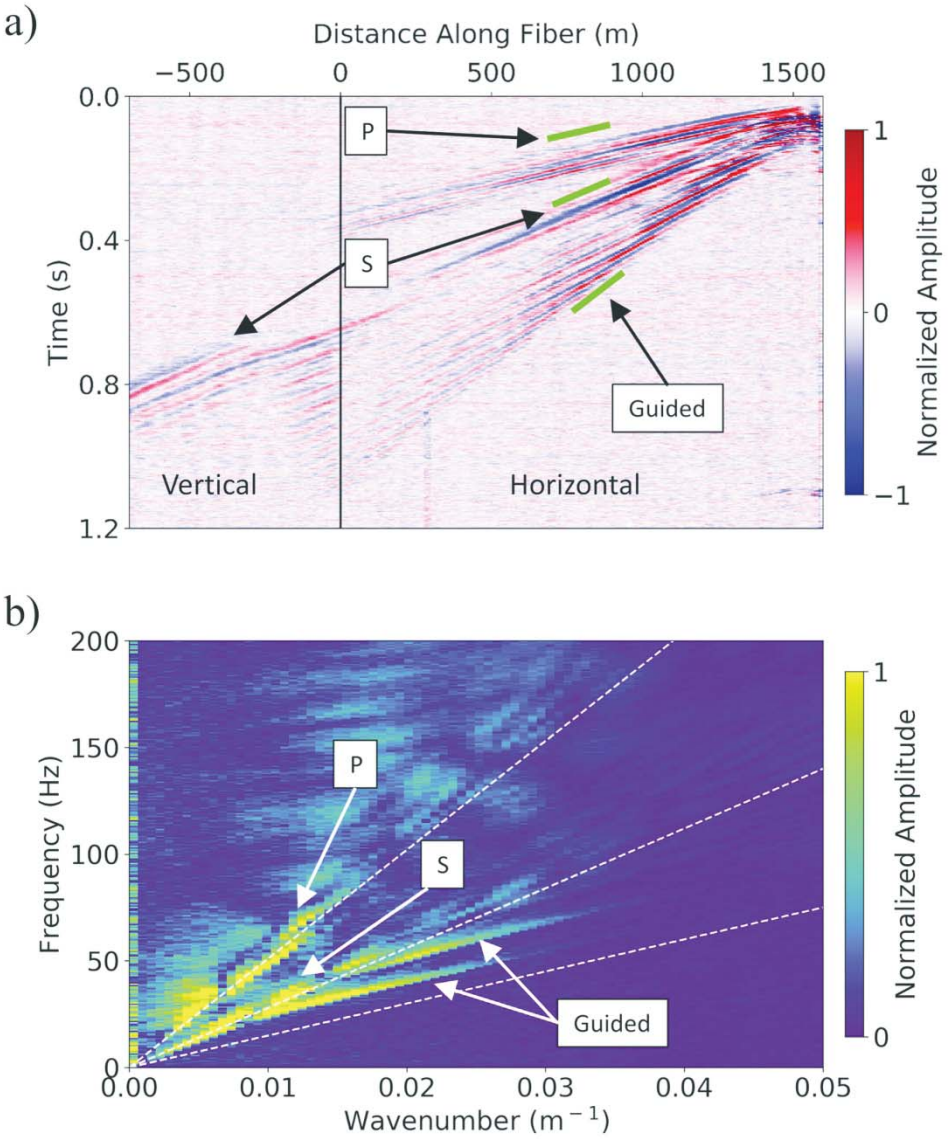

Figure 1. (a) The DAS seismic profile of an example microseismic event along the fiber in an L-shape monitor well. The black solid vertical line denotes the heel of the well. (b) The frequency-wavenumber spectrum of the horizontal section of the DAS record. Body waves and guided waves are marked. Green line segments in (a) and white dashed lines in (b) mark rough estimates of body P-wave velocity (5100 m/s), body S-wave velocity (2800 m/s), and guided wave group velocity (1500 m/s).

84x99mm (600 x 600 DPI)

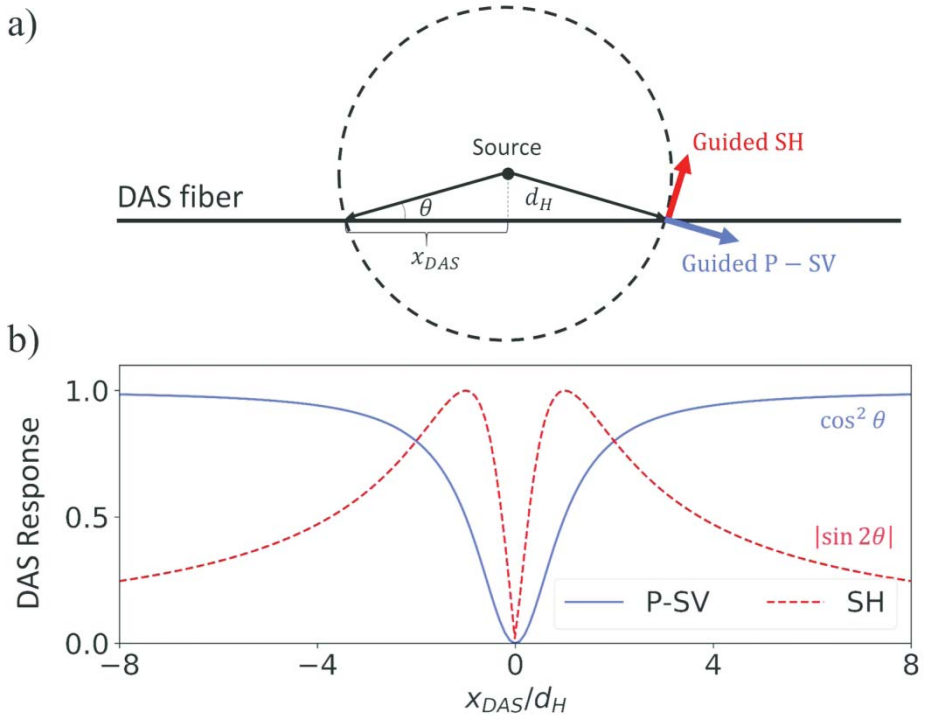

Figure 2. (a) Schematic map view diagram of the propagation geometry of the cylindrical guided waves and (b) the directional response of DAS to different types of guided waves along the DAS fiber.

84x64mm (600 x 600 DPI)

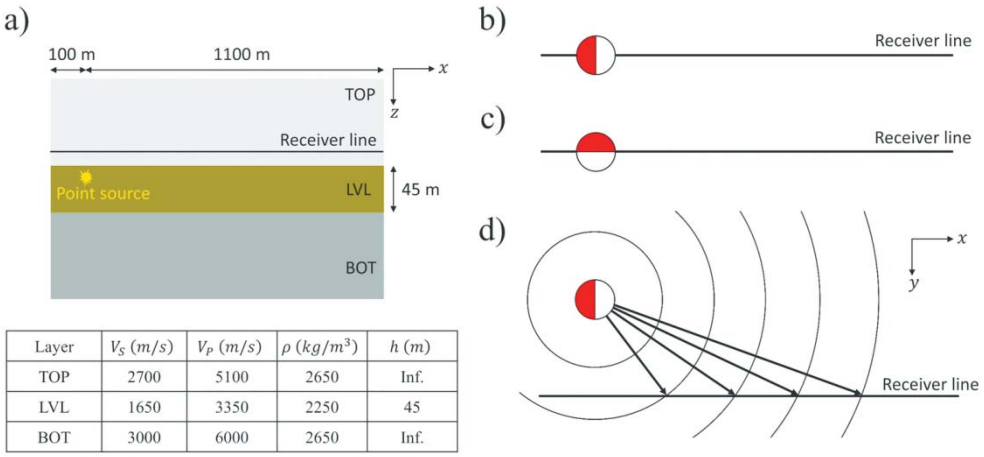

Layer	$V_S\ (m/s)$	$V_P\ (m/s)$	$\rho\ (kg/m^3)$	$h\ (m)$
TOP	2700	5100	2650	Inf.
LVL	1650	3350	2250	45
BOT	3000	6000	2650	Inf.

Figure 3. (a) Cross-section of the three-layered model (not to scale) and parameter summary for 3-D wavefield modeling. (b) Zero-*y*-offset double-couple point source with an M_{xz} excitation term. (c) Zero-*y*-offset double-couple point source with an M_{yz} excitation term. (d) Double-couple source with 200 m horizontal *y*-offset from the receiver line. (b-d) are map views of horizontal source-receiver layouts.

135x76mm (300 x 300 DPI)

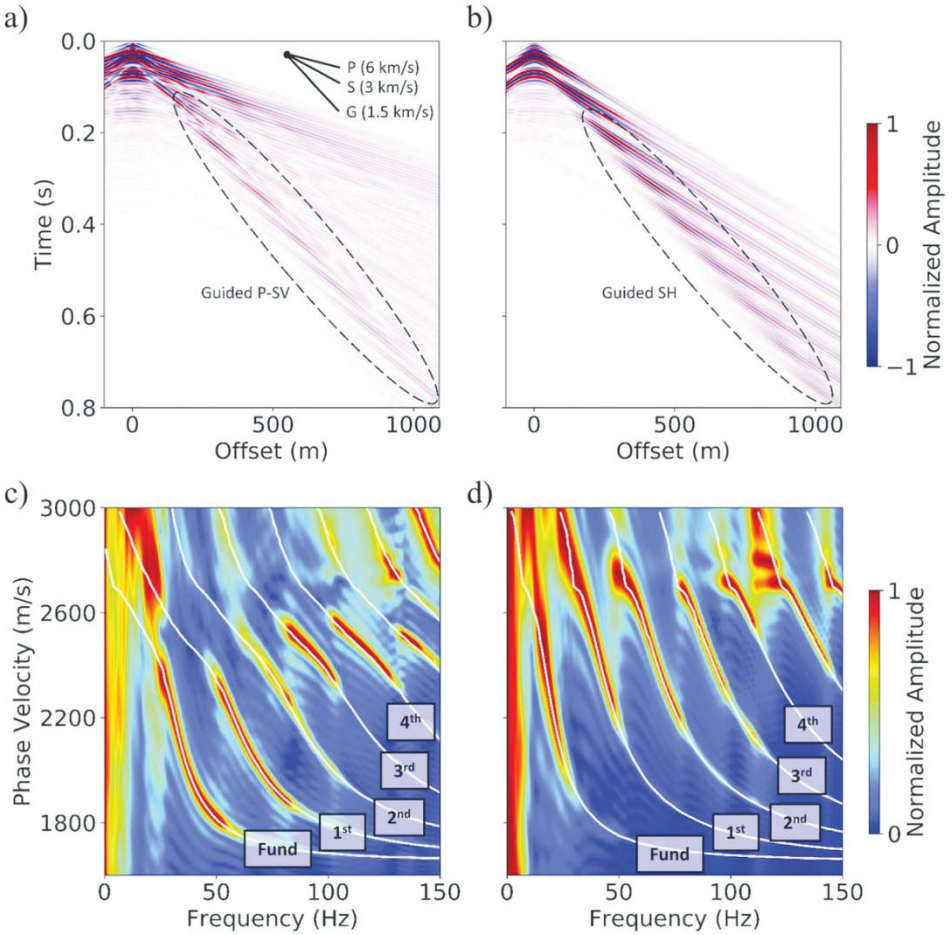

Figure 4. Synthetic seismic profiles of the isotropic model showing (a) *x*-component particle velocity of the M_{xz} experiment (Figure 3b) and (b) *y*-component particle velocity of the M_{yz} experiment (Figure 3c). Guided waves are highlighted by the black dashed ellipses. In (a), we observe P-SV modes, whereas in (b) SH modes are present. Reference travel velocities of different seismic modes are provided in (a). The corresponding dispersion images are shown in (c) and (d), respectively. White solid curves denote the theoretical multimodal dispersion curves obtained with the propagator matrix method. Mode numbers from fundamental to fourth are marked.

110x105mm (300 x 300 DPI)

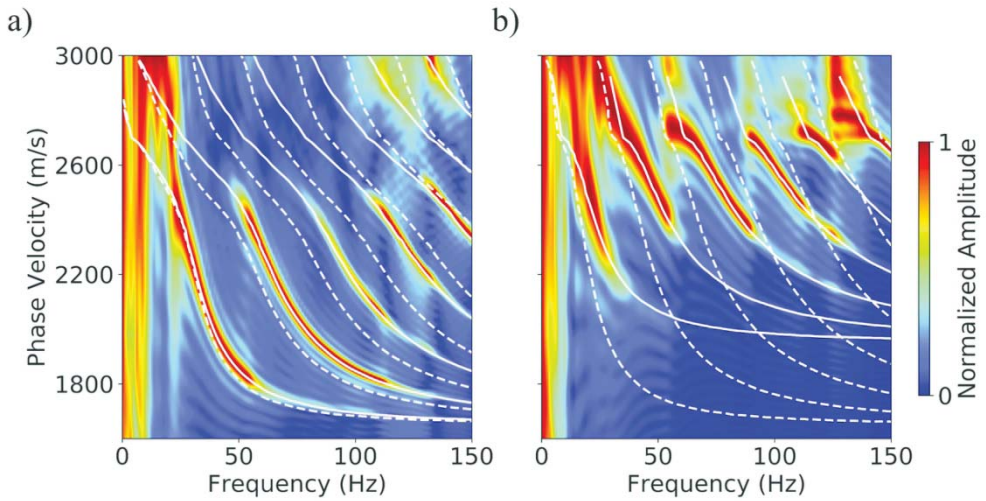

Figure 5. Dispersion images of the VTI model for synthetic (a) guided P-SV and (b) guided SH waves. White solid curves denote the theoretical multimodal dispersion curves of the VTI model. White dashed curves are the theoretical dispersion curves of the isotropic model for comparison.

110x59mm (300 x 300 DPI)

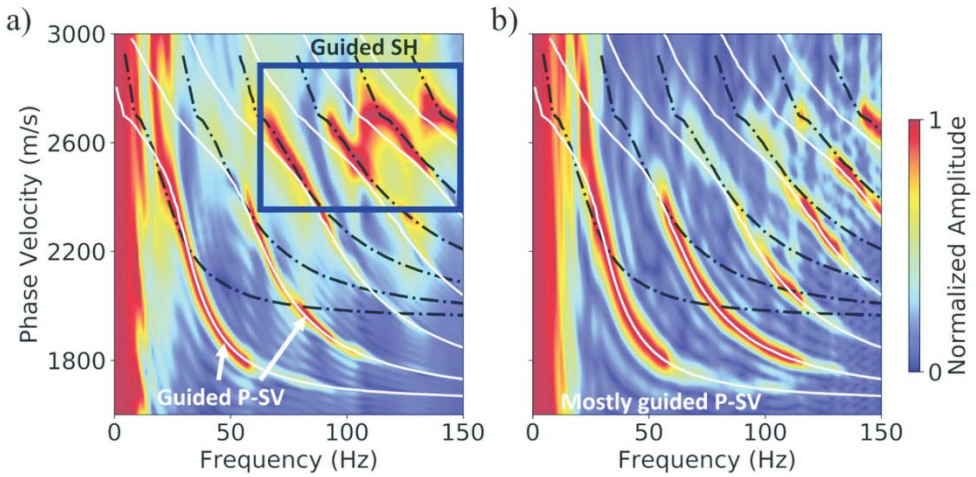

Figure 6. Dispersion images calculated from (a) the entire synthetic DAS records and (b) the long-offset synthetic DAS records. The DAS fiber is offset horizontally by 200 m from the source. White solid and black dash-dotted curves are theoretical dispersion curves of guided P-SV and SH waves, respectively, of the VTI LVL model. In (a), the fundamental and first P-SV modes are marked by white arrows, and the guided SH modes are highlighted by a black rectangle.

110x62mm (300 x 300 DPI)

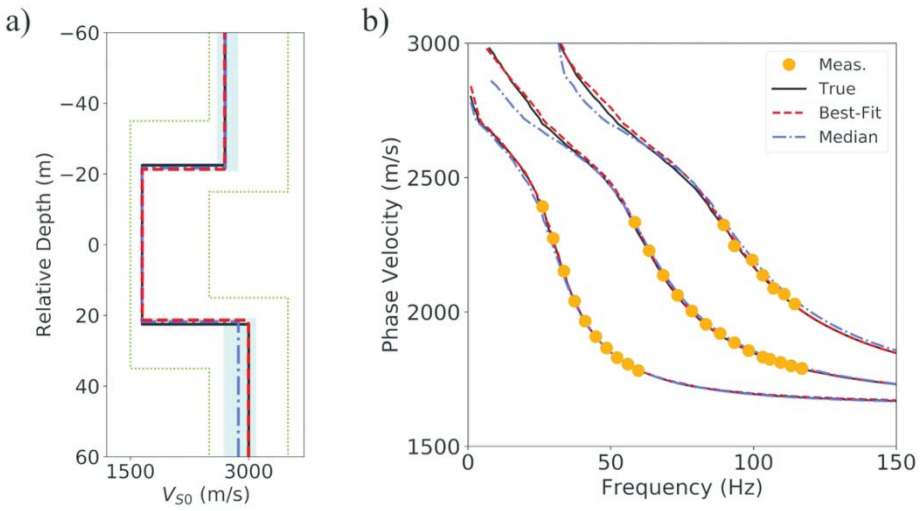

Figure 7. (a) Comparison of the V_{S0} profiles of the true VTI model (black), the best-fitting model (red dashed) and the median model of the best-fitting ensemble (blue dash-dotted). Light blue area represents the uncertainty range of the best-fitting ensemble. Green dotted lines mark the parameter boundaries for the Monte Carlo inversion. (b) Dispersion picks of the synthetic guided P-SV waves (orange) and the theoretical dispersion curves computed from the three models in (a).

110x62mm (300 x 300 DPI)

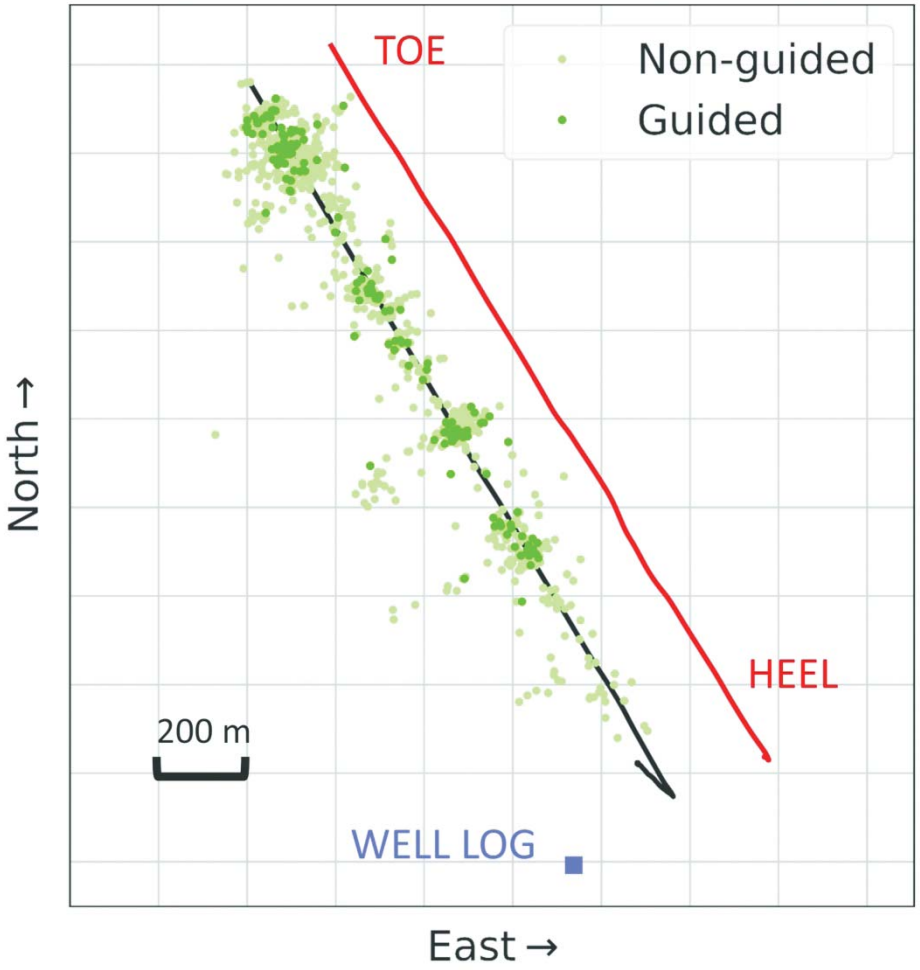

Figure 8. Map view of the microseismic events that occurred during the hydraulic fracturing operations in the Eagle Ford project. Locations were obtained from surface geophone processing. Events are color-coded to indicate whether energetic guided waves are observed (Huff et al., 2020). The horizontal section of the DAS monitor well (red curve), the horizontal section of the treatment well (black curve), and a vertical well (blue square) that was logged are also shown.

84x84mm (600 x 600 DPI)

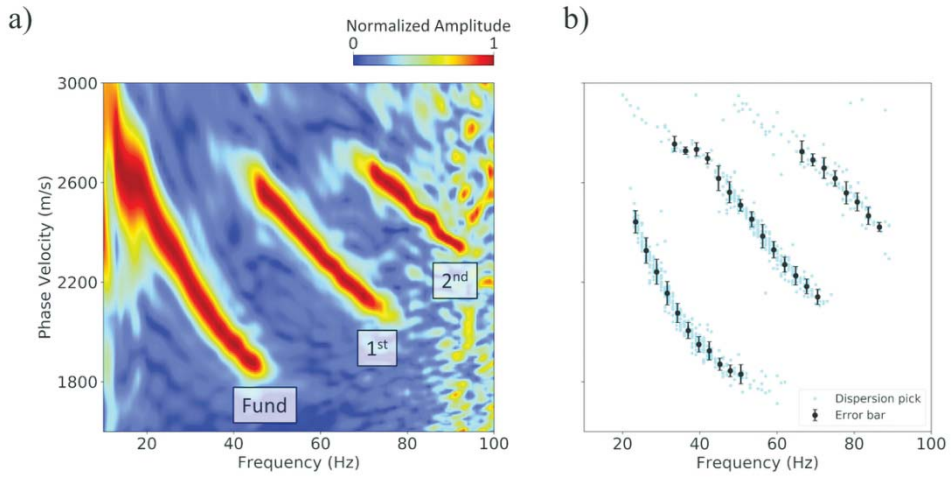

Figure 9. (a) Normalized dispersion image of the guided waves of a microseismic event example in the Eagle Ford project. Three trends of energy peaks are marked as fundamental, first higher, and second higher modes. (b) Dispersion picks of 17 microseismic events excited near the toe of the monitor well and displaying clear guided wave signals.

110x58mm (300 x 300 DPI)

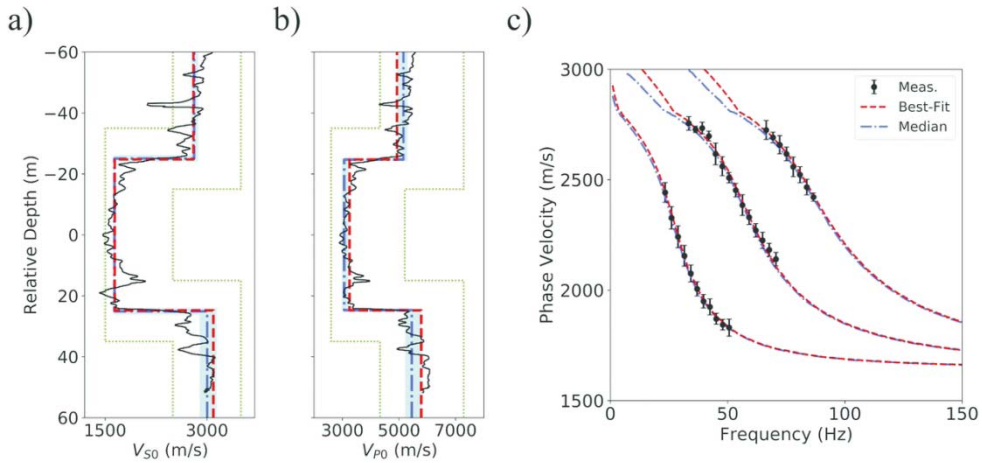

Figure 10. (a) The V_{S0} profile and (b) the V_{P0} profile of the best-fit 1-D model (red dashed) and the median model of the equivalent ensemble (blue dash-dotted). Light blue area shows the uncertainty range. Green dash-dotted curves are parameter boundaries for inversion. The sonic log profile (black solid) is shown for comparison. (c) Theoretical dispersion curves of guided P-SV waves of the best-fit model and the median model of the equivalent ensemble. Dispersion measurements of the Eagle Ford microseismic guided waves (black symbols) are shown for comparison.

110x57mm (300 x 300 DPI)

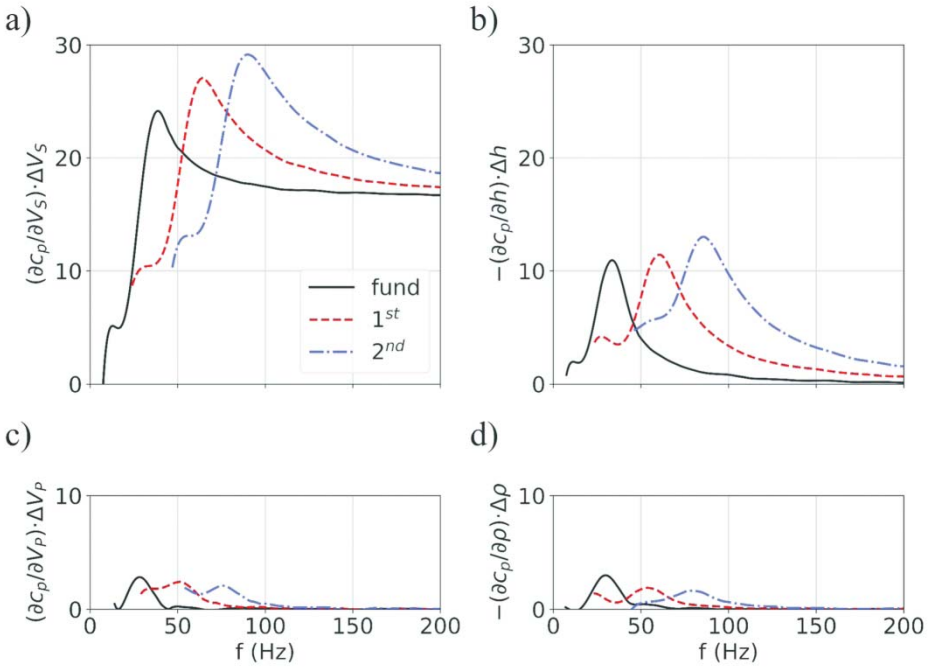

Figure 11. Sensitivity of the fundamental, first higher, and second higher modes of the guided P-SV waves with respect to (a) ΔV_S, (b) Δh, (c) ΔV_P, and (d) $\Delta \rho$, each of which is a 1% variation of the corresponding parameter compared to the reference model.

84x59mm (600 x 600 DPI)

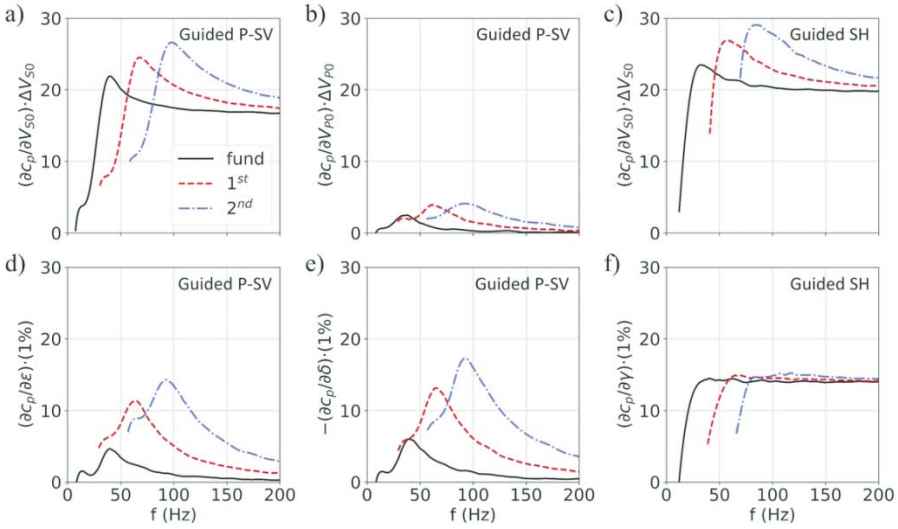

Figure 12. Sensitivity of the fundamental, first, and second guided wave modes to variation of wave velocities (a-c) and Thomsen parameters (d-f) in the LVL. Guided P-SV modal curves are sensitive to (a) vertical S-wave velocity, (b) vertical P-wave velocity, (d) ε, and (e) δ, while guided SH modal curves are sensitive to (c) vertical LVL S-wave velocity and (f) γ.

110x62mm (300 x 300 DPI)

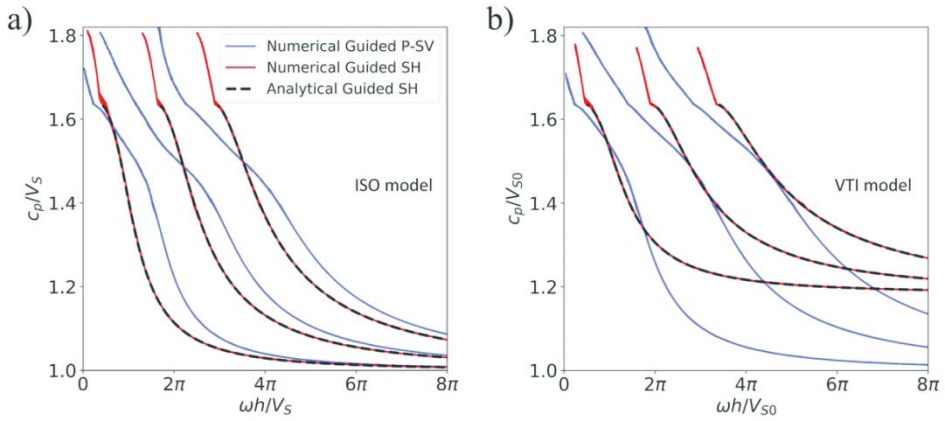

Figure 13. Dimensionless multimodal dispersion curves of (a) the isotropic models and (b) the VTI models. Each numerically calculated dispersion curve is a stack of overlapping curves calculated from a set of models with various LVL thickness ranging from 33 m to 57 m with 4 m stepping. The analytical solutions for guided SH modes are plotted for comparison.

110x51mm (300 x 300 DPI)

DATA AND MATERIALS AVAILABILITY

Data associated with this research are confidential and cannot be released.